Gravitational lensing by a generalised-NFW halo via the Fox H-function and its application to the super-NFW

Daniel Alexdy Torres-Ballesteros* and Leonardo Castañeda

Observatorio Astronómico Nacional, Universidad Nacional de Colombia, Carrera 30 Calle 45-03, P.A. 111321 Bogotá, Colombia

Accepted XXX. Received YYY; in original form ZZZ

ABSTRACT

We present an analytical framework for a family of axisymmetric gravitational lenses, in which we express the lensing properties in terms of the Fox H-function. We apply this framework to a generalised-NFW (gNFW) profile, where we provide the power series representation of the Fox H-functions involved, and explore their performance and accuracy. From these power series we show that the corresponding Fox H-functions reduce to simple expressions in terms of the Gauss hypergeometric function. We apply these results to the particular case of the super-NFW (sNFW) profile, obtaining simpler expressions, this time in terms of complete elliptic functions (which are easier to work with). When the number of images formed is maximum, the sum of their signed magnifications denoted as I, is constant for several lenses. We study its behaviour for the sNFW, NFW and Hernquist lenses, and show that for a fixed κ_0 (characteristic convergence), in general, I is not constant ($I_{\min} \le I \le I_{\max}$), as it exhibits a strong dependence on the source position inside the radial caustic. The boundaries depend on κ_0 (and so does the average $\langle I \rangle$). Our numerical experiments suggest that for these lenses $I_{\min} \to 1$ as κ_0 increases, and $I \to 1$ as $\kappa_0 \to \infty$. Additionally, I is constant only for a specific κ_0 , which is different for each model.

Key words: gravitational lensing: strong – gravitational lensing: weak – galaxies: haloes – methods: analytical.

1 INTRODUCTION

In our current understanding of the Universe, the dark sector contributes to about 95% of its content. The two dark components, known as dark energy and dark matter, are fundamental to our ΛCDM paradigm. One success of this paradigm is its ability to account for primordial density fluctuations that are amplified by the expansion of the Universe and, when they reach a critical value, collapse into dark matter haloes. Understanding how these dark matter haloes form and evolve is one of the most important tasks in cosmology and astrophysics. Gravitational lensing stands as a fundamental tool to unveil the nature of this dark sector at different scales (see e.g., Bartelmann & Schneider (2001); Munshi et al. (2008); Hoekstra & Jain (2008); Ellis (2010); Huterer (2010); Massey et al. (2010); Umetsu (2020); Natarajan et al. (2024)).

When we attempt to model astrophysical systems such as galaxies, galaxy groups, or galaxy clusters as gravitational lenses, fitting observational data is required. This can be done, for instance, using MCMC algorithms (or algorithms of similar nature), which require repeated evaluation of the lensing properties for the different components of such systems (e.g., Jullo et al. (2007); Oguri (2010)). This process is computationally expensive and time-consuming, especially when numerical integration is necessary (which scales with the complexity of the mass distributions). If the analytical properties of a required gravitational lens model are unavailable, an efficient alternative to numerical integration is to develop fast calculations methods. For example, Oguri (2021) proposed the superposition of cored steep

ellipsoids to compute the lensing properties for elliptic NFW and elliptic Hernquist lenses, an approach that he implemented in GLAFIC (Oguri 2010). Therefore, we aim to derive analytical expressions for the lensing properties of the generalised-NFW (gNFW) profile proposed by Evans & An (2006), a spherically symmetric profile defined as

$$\rho(r) = \frac{(n-2)\phi_0}{4\pi G r_0^2} \frac{1}{(r/r_0)(1+r/r_0)^{n-1}},\tag{1}$$

where r_0 is a length scale, ϕ_0 is the depth of the potential well, and n > 2. For this mass distribution the logarithmic slope takes the form

$$\frac{d\ln\rho}{d\ln r} = -1 + \frac{(1-n)(r/r_0)}{(1+r/r_0)},\tag{2}$$

where we can show that the gNFW satisfies $\rho(r) \propto r^{-1}$ as we approach to the centre $(r \ll r_0)$, while it falls off like $\rho(r) \propto r^{-n}$ when $r \gg r_0$.

This family of mass distributions includes as special cases the NFW for n = 3 (Navarro et al. 1997), Hernquist for n = 4 (Hernquist 1990), and super-NFW (sNFW) for n = 7/2 (Lilley et al. 2018a). In Fig. 1 we can see that for these three profiles the density changes at the same rate towards the centre (as any profile described by the gNFW). Towards the outskirts, however, the sNFW falls off faster than the NFW but slower than the Hernquist profile (precisely one of the motivations for defining the sNFW). Lilley et al. (2018a) showed that the sNFW is at least as good as the NFW in reproducing haloes extracted from N-body simulations, with the added advantage that the sNFW has a finite total mass. Additionally, the sNFW provides a better approximation to the surface brightness of elliptical galaxies and bulges in disc galaxies than the Hernquist profile. It can also be

^{*} E-mail:daatorresba@unal.edu.co

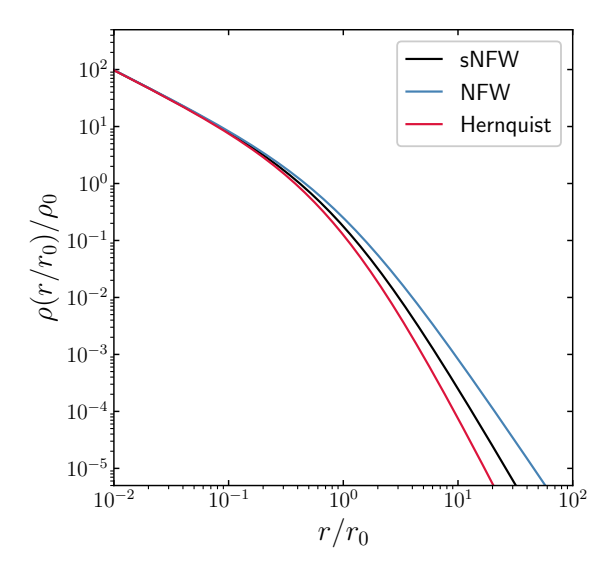


Figure 1. Normalised volumetric mass density given for the sNFW (black), NFW (blue), and Hernquist (red) profiles. Here, $\rho_0 = (n-2)\phi_0/(4\pi G r_0^2)$ is the characteristic density.

easily extended to distorted profiles beyond spherical symmetry (e.g., flattened or triaxial profiles), as it facilitates the constructions of a basis for a biorthogonal expansion of the potential-density pair. For further details, we refer the reader to Lilley et al. (2018a,b) and the references therein.

For the description of the gNFW (1) as a gravitational lens, the direct evaluation of the required integrals (see Sec. 2) is not necessarily evident or trivial. Fortunately, the Mellin transform (see Appendix A) and the Fox *H*-function (see Appendix B), working together, provide an elegant and powerful combination that allows us to achieve our goal. Within the astronomical context, this combination has been successfully applied, for instance, to the deprojection of the Sérsic surface brightness model (Baes & Gentile 2011; Baes & van Hese 2011), and to express the gravitational lensing properties of the Einasto profile (Retana-Montenegro et al. 2012a,b) and the Dekel-Zhao profile (Freundlich et al. 2020).

This work is structured as follows: In Sec. 2 we establish notation and present the necessary elements of gravitational lensing for axisymmetric lenses. Then, in Sec. 3, we derive the lensing properties for a particular family of lenses via the Fox *H*-function, which we apply to the gNFW profile in Sec. 4. In Sec. 5, we focus on the sNFW, where we derive its analytical lensing properties. Also, for the sNFW, NFW and Hernquist lenses, when the number of images produced by these lenses reaches its maximum (three in this case), we study the behaviour of the sum of their signed magnifications. Finally, a summary and conclusions are presented in Sec. 6.

2 GRAVITATIONAL LENSING BASICS

In this section we describe some aspects of the gravitational lensing effect within the framework of the thin lens approximation. In particular, we focus on spherically symmetric mass distributions, which generate axisymmetric lenses. With respect to the general formalism for axisymmetric gravitational lenses, we mainly follow Schneider et al. (1992, 2006) unless otherwise stated. An alternative approach to lenses with this symmetry can be found in, e.g., Hurtado et al. (2014).

Within the thin lens approximation, the lens is characterised by the

projected mass distribution along the line of sight (denoted by the coordinate z), whose surface mass density can be written as

$$\Sigma(\xi) = 2 \int_0^\infty \rho(\xi, z) dz,\tag{3}$$

where $\rho(r)$ is the spherically symmetric mass distribution, with $r^2 = \xi^2 + z^2$, and ξ represents the radial coordinate on the lens plane (perpendicular to line of sight). Introducing the dimensionless radius $x = \xi/\xi_0$, where ξ_0 serves as an adequate normalisation length scale, the projected mass enclosed by the lens within a radius x (equivalent to the mass enclosed by an infinite cylinder of such radius) takes the form

$$M(x) = 2\pi \xi_0^2 \int_0^x \chi \Sigma(\chi) d\chi. \tag{4}$$

Once we have a lens with redshift z_l , the bending of light is ruled by the lens equation, a two-dimensional vector equation that for a given source with redshift $z_s > z_l$, links its true position η on the source plane to its apparent position ξ on the lens plane. The corresponding deviation is given by the deflection angle $\hat{\alpha}$. Axisymmetric lenses satisfy the condition that η , ξ , and $\hat{\alpha}$ are collinear, allowing us to drop the azimuthal dependence and keep only their radial component, leading to the one-dimensional lens equation

$$y = x - \alpha(x),\tag{5}$$

where $y = \eta/\eta_0$ with $\eta_0 = (D_s/D_l)\xi_0$, and

$$\alpha(x) = \frac{D_l D_{ls}}{D_s \xi_0} \hat{\alpha}(x) = \frac{2}{\Sigma_{\rm cr} x} \int_0^x \chi \Sigma(\chi) d\chi = \frac{M(|x|)}{\pi \xi_0^2 \Sigma_{\rm cr} x} \tag{6}$$

is the radial component of the scaled deflection angle, which we will refer to as the deflection angle for simplicity. Note that

$$\Sigma_{\rm cr} = \frac{c^2 D_s}{4\pi G D_l D_{ls}} \tag{7}$$

is the critical (lens) density. The gravitational lensing effect is mediated by the angular diameter distances $D_s = D(z_s)$, $D_l = D(z_l)$, and $D_{ls} = D(z_l, z_s)$, which correspond to the distances between the observer and source, observer and lens, and lens and source, respectively.

The lens equation (5) is non-linear in x, meaning that for a given source position y, multiple solutions x may exist, each corresponding to a distinct apparent image. The deflection angle (6) is expressed in terms of M(|x|) to account for possible negative solutions. Beyond producing multiple images, the lens also distorts in both shape and size the apparent contour of background sources. The isotropic deformations (scaling), and anisotropic deformations (change in the apparent ellipticity) are described by the convergence

$$\kappa(x) = \frac{\Sigma(x)}{\Sigma_{\rm cr}},\tag{8}$$

and shear, respectively. For axisymmetric lenses the shear is given by (Miralda-Escude 1991)

$$\gamma(x) = \frac{\overline{\Sigma}(x) - \Sigma(x)}{\Sigma_{\rm cr}},\tag{9}$$

with

$$\overline{\Sigma}(x) = \frac{2}{x^2} \int_0^x \chi \Sigma(\chi) d\chi = \frac{M(x)}{\pi \xi_0^2 x^2}$$
 (10)

being the mean surface mass density within x. For axisymmetric lenses, (9) equals the average tangential shear taken over a circle of radius x. Some applications of the tangential shear con be found in,

e.g., Bartelmann (1995); Nakajima et al. (2009); Giocoli et al. (2014). A stronger signal is obtained after taking the mean value of (9) up to a given radius x, which leads to the mean shear

$$\overline{\gamma}(x) = \frac{2}{x^2} \int_0^x \chi \gamma(\chi) d\chi. \tag{11}$$

The gravitational lensing effect can also be described through a scalar potential known as the deflection potential, which for axisymmetric lenses takes the form

$$\psi(x) = \frac{2}{\Sigma_{\rm cr}} \int_0^x \chi \Sigma(\chi) \ln\left(\frac{x}{\chi}\right) d\chi. \tag{12}$$

This potential relates to the deflection angle and convergence through

$$\alpha(x) = \psi'(x)$$
 and $2\kappa(x) = \frac{\psi'(x)}{x} + \psi''(x)$, (13)

where the prime indicates derivatives with respect to x.

Now, for axisymmetric lenses we derive an explicit relation between the mean shear and the deflection potential. From (9), the mean shear (11) can be written as $\overline{\gamma}(x) = (\widetilde{\Sigma}(x) - \overline{\Sigma}(x))/\Sigma_{\rm cr}$, where $\overline{\Sigma}(x)$ is given by (10), and

$$\widetilde{\Sigma}(x) = \frac{2}{x^2} \int_0^x \chi \overline{\Sigma}(\chi) d\chi = \frac{2}{\pi \xi_0^2 x^2} \int_0^x \frac{M(\chi)}{\chi} d\chi.$$
 (14)

Using (6) and (13), and considering that the integration in (14) is carried out over a non-negative domain, the integrand can be expressed in terms of the deflection potential as

$$\frac{M(\chi)}{\chi} = \pi \xi_0^2 \Sigma_{\rm cr} \psi'(\chi). \tag{15}$$

Thus, after substituting this result into (14), the mean shear becomes

$$\overline{\gamma}(x) = \frac{2\Delta\psi(x)}{x^2} - \frac{M(x)}{\pi\xi_0^2 \Sigma_{\text{cr}} x^2} = \frac{2\Delta\psi(x)}{x^2} - \frac{\psi'(x)}{x},\tag{16}$$

with $\Delta \psi(x) = \psi(x) - \psi(0)$. Note that for (16) to remain finite, $\psi(0)$ must to be well defined. Expression (16) has been used, for example, in Martel & Shapiro (2003).

3 A GENERAL LENS VIA THE FOX H-FUNCTION

Let us consider a general lens whose surface mass density can be written in terms of the Fox *H*-function as

$$\Sigma(x) = \Sigma_0 x^a \underbrace{\left(\frac{1}{2\pi i} \int_{\mathcal{L}} \Theta_{\Sigma}(v) x^{-bv} dv\right)}_{\text{Fox } H\text{-function, see (B1)}},$$
(17)

where $a, b \in \mathbb{R}$ with $b \neq 0$, $\Theta_{\Sigma}(v)$ satisfies (B2), and Σ_0 is a constant that depends on the physical properties of the lens, known as the characteristic surface mass density.

Here, we show that relation (16) holds true for lenses that satisfy (17) (including the gNFW), without requiring explicit knowledge of $\psi(0)$. To do this, we evaluate (14) and assess whether it can be expressed in terms of the deflection potential. First of all, we need the projected mass, which can be obtained by substituting (17) into (4), such that

$$M(x) = 2\pi \xi_0^2 \Sigma_0 \left(\frac{1}{2\pi i} \int_{\Gamma} \int_0^x \Theta_{\Sigma}(v) \chi^{1+a-bv} d\chi dv \right), \tag{18}$$

which, once we perform the integration with respect to χ becomes

$$M(x) = \frac{2\pi\xi_0^2 \Sigma_0 x^{2+a}}{b} \left(\frac{1}{2\pi i} \int_{\mathcal{L}} \Theta_M(v) x^{-bv} dv \right),\tag{19}$$

with

$$\Theta_{M}(v) = \frac{1}{\frac{2+a}{b} - v} \Theta_{\Sigma}(v) = \frac{\Gamma\left(\frac{2+a}{b} - v\right)}{\Gamma\left(\frac{2+a+b}{b} - v\right)} \Theta_{\Sigma}(v). \tag{20}$$

We work with $\left(\frac{2+a}{b} - v\right)$ instead of (2+a-bv) for convenience. Now, by substituting (19) into (14) and following the same procedure described above, we obtain

$$\widetilde{\Sigma}(x) = \frac{4\Sigma_0 x^a}{b^2} \left(\frac{1}{2\pi i} \int_{\Gamma} \Theta_{\widetilde{\Sigma}}(v) x^{-bv} dv \right),\tag{21}$$

with

$$\Theta_{\widetilde{\Sigma}}(v) = \frac{1}{\frac{2+a}{b} - v} \Theta_{M}(v) = \frac{\Gamma\left(\frac{2+a}{b} - v\right)^{2}}{\Gamma\left(\frac{2+a+b}{b} - v\right)^{2}} \Theta_{\Sigma}(v). \tag{22}$$

Similarly, if we substitute (21) into (12) and integrate with respect to χ (analogous to what we did to get (19)), the deflection potential takes the form

$$\psi(x) = \frac{2\kappa_0 x^{2+a}}{b^2} \left(\frac{1}{2\pi i} \int_{f} \Theta_{\psi}(v) x^{-bv} dv \right), \tag{23}$$

where $\kappa_0 = \Sigma_0 / \Sigma_{cr}$ is the characteristic convergence, and

$$\Theta_{\psi}(v) = \frac{1}{\left(\frac{2+a}{b} - v\right)^2} \Theta_{\Sigma}(v) = \frac{\Gamma\left(\frac{2+a}{b} - v\right)^2}{\Gamma\left(\frac{2+a+b}{b} - v\right)^2} \Theta_{\Sigma}(v). \tag{24}$$

Then, from comparing (21) and (23) it is clear that

$$\widetilde{\Sigma}(x) = 2\Sigma_{\rm cr}\psi(x)/x^2. \tag{25}$$

This result implies that for any lens with surface mass density described by (17), its deflection potential satisfies $\psi(0) = 0$, which is equivalent to have $\Delta \psi(x) = \psi(x)$. As outlined in Sec. 2, it is clear that, from the surface mass density (17), projected mass (19), and deflection potential (23), we have all we need to describe our general lens.

Now, we evaluate the total mass $M_{\infty} = M(x \to \infty)$ enclosed by the lens. To do so, we use (18), where we apply the change of variable $w = \chi^b$ and take $x \to \infty$. If we consider b > 0, the total mass can be written as

$$M_{\infty} = \int_0^{\infty} m(w)w^{(2+a-b)/b} dw,$$
 (26)

where

$$m(w) = \frac{1}{2\pi i} \int_{\mathcal{L}} \mathcal{M}(v) w^{-v} dv = \mathfrak{M}_{\mathcal{M}}^{-1}(w)$$
 (27)

turns out to be the inverse Mellin transform (see (A2)) of

$$\mathcal{M}(v) = 2\pi \xi_0^2 \Sigma_0 \Theta_{\Sigma}(v) / b, \tag{28}$$

which, in turn, is equal to the Mellin transform (see (A1)) of m(w). This is.

$$\mathfrak{M}_m(v) = \int_0^\infty m(w)w^{v-1}dw = \mathcal{M}(v). \tag{29}$$

By comparing (26) and (29), we obtain a simple expression for M_{∞} in terms of (28). We then perform an analogous process for b < 0 and combine both results into

$$M_{\infty} = \begin{cases} \mathcal{M}\left(\frac{2+a}{b}\right) & \text{if } b > 0\\ -\mathcal{M}\left(\frac{2+a}{b}\right) & \text{if } b < 0 \end{cases}$$
(30)

4 THE GENERALISED-NFW HALO AS A GRAVITATIONAL LENS

If we want to apply to the gNFW the framework presented in the previous section, we need to show first that its surface mass density satisfies (17). To do this, we follow the methodology outlined in Appendix A. We proceed by expressing the surface mass density as the Mellin convolution $f_1 \star f_2$ (as defined in (A3)) between two suitable functions, f_1 and f_2 . The definition of the surface mass density given in (3) is not suited for the job, instead, it can be rewritten as the Abel integral

$$\Sigma(\xi) = 2 \int_{\xi}^{\infty} \frac{\rho(r)rdr}{\sqrt{r^2 - \xi^2}},\tag{31}$$

which, for the gNFW with normalisation length $\xi_0 = r_0$ and dimensionless radius $x = \xi/r_0$, reads

$$\Sigma(x) = \frac{(n-2)\phi_0}{2\pi G r_0} \int_x^{\infty} \frac{dt}{(1+t)^{n-1} \sqrt{t^2 - x^2}},$$
 (32)

where $t = r/r_0$. For (32) the required functions f_1 and f_2 take the form

$$f_1(h=t) = \frac{(n-2)\phi_0}{2\pi G r_0} \frac{h}{(1+h)^{n-1}},\tag{33}$$

and

$$f_2(h = x/t) = \begin{cases} \frac{h}{x\sqrt{1 - h^2}} & \text{if } 0 \le h < 1\\ 0 & \text{otherwise} \end{cases}$$
 (34)

The next step requires the Mellin transform \mathfrak{M} (as defined in (A1)) of f_1 and f_2 , which are

$$\mathfrak{M}_{f_1}(u) = \frac{(n-2)\psi_0}{2\pi Ga} \frac{\Gamma(n-2-u)\Gamma(1+u)}{\Gamma(n-1)}$$
(35)

and

$$\mathfrak{M}_{f_2}(u) = \frac{\sqrt{\pi}}{2x} \frac{\Gamma\left(\frac{1+u}{2}\right)}{\Gamma\left(1+\frac{u}{2}\right)},\tag{36}$$

respectively. Since the surface mass density satisfies $\Sigma(x) = (f_1 \star f_2)(x)$, it can also be expressed following the definition in (A6). Therefore, we substitute (35) and (36) into (A6), and (for convenience) apply the change of variable v = 1 + u/2, leading to

$$\Sigma(x) = \Sigma_0 x \left(\frac{1}{2\pi i} \int_{\mathcal{L}} \Theta_{\Sigma}(v) x^{-2v} dv \right), \tag{37}$$

with

$$\Theta_{\Sigma}(v) = \frac{\Gamma(-1+2v)\Gamma(-\frac{1}{2}+v)\Gamma(n-2v)}{\Gamma(v)}$$
(38)

and

$$\Sigma_0 = \frac{(n-2)\phi_0}{2\sqrt{\pi}Gr_0\Gamma(n-1)}.$$
(39)

We can see that, with a = 1 and b = 2, the gNFW falls within the family of lenses defined by (17).

As outlined in Sec. 3, from (38) each $\Theta_i(v)$ (with i = M (20), ψ (24)) takes the form

$$\Theta_{M}(v) = \frac{\Gamma(-1+2v)\Gamma(-\frac{1}{2}+v)\Gamma(n-2v)\Gamma(\frac{3}{2}-v)}{\Gamma(v)\Gamma(\frac{5}{2}-v)},$$
(40)

$$\Theta_{\psi}(v) = \frac{\Gamma(-1+2v)\Gamma(-\frac{1}{2}+v)\Gamma(n-2v)\Gamma(\frac{3}{2}-v)^{2}}{\Gamma(v)\Gamma(\frac{5}{2}-v)^{2}}.$$
 (41)

We apply these results to the definition of the Fox H-function given in (B1), obtaining

$$\Sigma(x) = \Sigma_0 x H_{2,2}^{2,1} \left[x^2 \middle| (1 - n, 2), (0, 1) \middle| (-1, 2), (-\frac{1}{2}, 1) \right], \tag{42}$$

$$M(x) = \pi r_0^2 \Sigma_0 x^3 H_{3,3}^{2,2} \left[x^2 \left| (1 - n, 2), (-\frac{1}{2}, 1), (0, 1) \right| , (43) \right]$$

$$\psi(x) = \frac{\kappa_0 x^3}{2} H_{4,4}^{2,3} \left[x^2 \left| (1 - n, 2), (-\frac{1}{2}, 1), (-\frac{1}{2}, 1), (0, 1) \right| (-1, 2), (-\frac{1}{2}, 1), (-\frac{3}{2}, 1), (-\frac{3}{2}, 1) \right]. \tag{44}$$

Each of these Fox H-functions can be written in its short notation as

$$H_{2,2\Sigma}^{2,1}\left(x^{2},n\right), H_{3,3M}^{2,2}\left(x^{2},n\right), H_{4,4\psi}^{2,3}\left(x^{2},n\right),$$
 (45)

respectively. Thus, the convergence (8) and deflection angle (6) become

$$\kappa(x) = \kappa_0 x H_{2,2\Sigma}^{2,1} \left(x^2, n \right) \tag{46}$$

and

$$\alpha(x) = \frac{\kappa_0 |x|^3}{x} H_{3,3M}^{2,2} \left(x^2, n\right),\tag{47}$$

while the shear (9) and mean shear (16) are given by

$$\gamma(x) = \kappa_0 x \left(H_{3,3M}^{2,2} \left(x^2, n \right) - H_{2,2\Sigma}^{2,1} \left(x^2, n \right) \right) \tag{48}$$

and

$$\overline{\gamma}(x) = \kappa_0 x \left(H_{4,4\psi}^{2,3} \left(x^2, n \right) - H_{3,3M}^{2,2} \left(x^2, n \right) \right). \tag{49}$$

From either the power series listed in Sec. 4.2 or the expression in Sec. 4.3, it can be shown that, in the limit as $x \to 0$, the surface mass density and convergence diverge. The projected mass, deflection angle, and deflection potential satisfy $M(x \to 0) = \alpha(x \to 0) = \psi(x \to 0) = 0$, and for the shear and mean shear we get

$$\gamma(x \to 0) = \overline{\gamma}(x \to 0) = \frac{\kappa_0 \Gamma(n-1)}{2\sqrt{\pi}}.$$
 (50)

Additionally, substituting (38) and (39) into (30) yields the total mass enclosed by the gNFW lens, which turns out to be

$$M_{\infty} = \mathcal{M}(3/2) = \frac{r_0(n-2)\Gamma(n-3)\phi_0}{G\Gamma(n-1)} = \frac{r_0\phi_0}{G(n-3)}.$$
 (51)

We can see that M_{∞} diverges or is negative for $2 < n \le 3$, but remains finite and positive for n > 3. This result is in agreement with the total mass reported by Evans & An (2006).

As a final remark, it is worth noting that there are exceptions to the rule, and for some mass distributions (with spherical symmetry) the Mellin technique simply does not work. For instance, that is the case with the Singular Isothermal Sphere (SIS). We elaborate a little bit more about this limitation in Appendix C.

4.1 Meijer G-function representation

The Fox H-function has not yet been implemented in most software used for numerical calculations. That is not the case of the Meijer G-function, which is implemented, for example, in MATHEMATICA

and PYTHON. Depending on the application in mind or the software being used, these implementations (on their current state) may be impractical. Nonetheless, the representation of (42)-(44) in terms of the Meijer *G*-function might be handy. Since the Meijer *G*-function is a special case of the Fox *H*-function (see Appendix B), from Gausss multiplication formula (Abramowitz & Stegun 1972)

$$\Gamma(kx) = (2\pi)^{(1-k)/2} k^{kx-1/2} \prod_{i=0}^{k-1} \Gamma\left(x + \frac{j}{k}\right),\tag{52}$$

where $k \in \mathbb{Z}^+$, we can rewrite (38) as

$$\Theta_{\Sigma}(\nu) = \frac{2^{n-3}}{\pi} \Gamma\left(-\frac{1}{2} + \nu\right)^2 \Gamma\left(\frac{n+1}{2} - \nu\right) \Gamma\left(\frac{n}{2} - \nu\right),\tag{53}$$

which allows us to write (42)-(44) as

$$\Sigma(x) = \frac{2^{n-3} \Sigma_0 x}{\pi} G_{2,2}^{2,2} \left[x^2 \left| \frac{\frac{1-n}{2}, 1 - \frac{n}{2}}{-\frac{1}{2}, -\frac{1}{2}} \right| \right], \tag{54}$$

$$M(x) = 2^{n-3} r_0^2 \Sigma_0 x^3 G_{3,3}^{2,3} \left[x^2 \begin{vmatrix} \frac{1-n}{2}, 1 - \frac{n}{2}, -\frac{1}{2} \\ -\frac{1}{2}, -\frac{1}{2}, -\frac{3}{2} \end{vmatrix} \right], \tag{55}$$

$$\psi(x) = \frac{2^{n-4}\kappa_0 x^3}{\pi} G_{4,4}^{2,4} \left[x^2 \begin{vmatrix} \frac{1-n}{2}, 1 - \frac{n}{2}, -\frac{1}{2}, -\frac{1}{2} \\ -\frac{1}{2}, -\frac{1}{2}, -\frac{3}{2}, -\frac{3}{2} \end{vmatrix} \right]. \tag{56}$$

4.2 Power series representation

From what we have discussed so far, we require three independent representations of the Fox H-function (given in (45)). The domain in which these functions converge depends on the parameters Δ and δ (defined in (B5)), as detailed in Appendix B6. In our case, all three functions satisfy $\Delta=0$ and $\delta=1$, such that they are well-defined for $0 < x^2 < 1$ and $x^2 > 1$.

Regarding their power series representation, for each domain we need to evaluate the poles of the different Γ functions present in the numerator of each $\Theta_i(v)$ (with $i=\Sigma$ (38), M (40), ψ (41)). For $0 < x^2 < 1$ we consider functions of the form $\Gamma(b_j + B_j v)$, whose poles satisfy (B3). Similarly, for $x^2 > 1$ we consider (the remaining) functions of the form $\Gamma(1-a_j-A_j v)$, whose poles satisfy (B4). The general expansions considering poles up to third order are covered in (B7). In general, they depend not only on Γ functions, but also on the special functions ψ_0 and ψ_1 , known as the digamma and trigamma functions, respectively. Note that for (B7) to apply, there must be no overlap between the poles (B3) and the poles (B4). See Appendix B for further details on the Fox H-function and its power series representations.

4.2.1 Function
$$H_{2,2\Sigma}^{2,1}(x^2,n)$$

From (38), we have that within the domain $0 < x^2 < 1$, the poles are

$$\Gamma(b_j + B_j v) \longrightarrow \beta_1 = (1 - k_1)/2$$

$$\beta_2 = 1/2 - k_2,$$
 (57)

with $k_1, k_2 \in \mathbb{N}_0$ (keep this in mind). We have poles of second order when the constraint $\beta_1 = \beta_2$ is satisfied, which is equivalent to have $k_1 = 2k_2$. This constraint indicates that poles β_1 with k_1 even, and all poles β_2 are of second order. In consequence, poles β_1 with k_1 odd are simple. For $x^2 > 1$ we only have single poles of the form

$$\Gamma(1 - a_j - a_j v) \longrightarrow \alpha = (n+l)/2,$$
 (58)

with $l \in \mathbb{N}_0$.

The corresponding expansions on each domain are given below.

For
$$0 < x^2 < 1$$
 $(n > 2)$:

$$\frac{2^{n-3}}{\pi|x|} \sum_{k=0}^{\infty} \Gamma\left(\frac{n-1}{2} + k\right) \Gamma\left(\frac{n}{2} + k\right) \frac{x^{2k}}{(k!)^2} \left[2\psi_0(1+k) - \psi_0\left(\frac{n-1}{2} + k\right) - \psi_0\left(\frac{n}{2} + k\right) - \ln\left(x^2\right)\right]$$
(59)

For $x^2 > 1$ (n > 2):

$$\frac{1}{2} \sum_{l=0}^{\infty} \frac{(-1)^l}{l!} \frac{\Gamma(n-1+l) \Gamma\left(\frac{n-1+l}{2}\right)}{\Gamma\left(\frac{n+l}{2}\right)} |x|^{-(l+n)}$$

$$(60)$$

4.2.2 Function
$$H_{3,3M}^{2,2}(x^2,n)$$

From (40), we have that for $0 < x^2 < 1$, the required poles are identical to those in (57) and therefore satisfy the same multiplicity conditions. While for $x^2 > 1$ the poles are

$$\Gamma(1 - a_j - a_j v) \longrightarrow \alpha_1 = (n + l_1)/2$$

$$\alpha_2 = 3/2 + l_2, \tag{61}$$

with $l_1, l_2 \in \mathbb{N}_0$ (keep this in mind). We have poles of second order when the constraint $\alpha_1 = \alpha_2$ is satisfied, which equivalent to have

$$l_1 = 3 - n + 2l_2$$
 or $l_2 = (n - 3 + l_1)/2$. (62)

On the one hand, if $n \notin \mathbb{Z}$, from constraint (62) we have that all poles α_1 and α_2 are simple, since for a given l_2 the condition $l_1 \in \mathbb{N}_0$ is not satisfied. On the other hand, if $n \in \mathbb{Z}$, poles α_1 with l_1 satisfying $(n-3+l_1) \mod 2 = 0$ (where l_1 must be odd when n is even, and even when n is odd) are of second order, which is necessary for condition $l_2 \in \mathbb{N}_0$ to be satisfied in (62). Similarly, poles α_2 with $l_2 \ge (n-3)/2$ are of second order, which is the result of considering that $l_1 \ge 0$ in (62).

Consequently, poles α_1 are simple for any l_1 satisfying $(n-3+l_1) \, mod \, 2 \neq 0$ (where l_1 must be odd when n is odd, and even when n is even), as do poles α_2 with $0 \leq l_2 < (n-3)/2$. For instance, if we consider n=3, the conditions for getting poles of second order become $l_1 \, mod \, 2 = 0$ and $l_2 \geq 0$. This implies that poles α_1 with l_1 even, and all poles α_2 are of second order. While poles α_1 with l_1 odd are simple.

The corresponding expansions on each domain are given below.

For
$$0 < x^2 < 1 (n > 2)$$
:

$$\frac{2^{n-3}}{\pi|x|} \sum_{k=0}^{\infty} \Gamma\left(\frac{n-1}{2} + k\right) \Gamma\left(\frac{n}{2} + k\right) \frac{x^{2k}}{k!(k+1)!} \left[\psi_0(1+k) + \psi_0(2+k) - \psi_0\left(\frac{n-1}{2} + k\right) - \psi_0\left(\frac{n}{2} + k\right) - \ln\left(x^2\right)\right]$$
(63)

For $x^2 > 1$ (n > 2 and $n \notin \mathbb{Z})$:

$$\sum_{l=0}^{\infty} \frac{(-1)^l}{l!} \frac{\Gamma(n-1+l)\Gamma(\frac{n-1+l}{2})}{\Gamma(\frac{n+l}{2})} \frac{|x|^{-(l+n)}}{(3-n-l)} + \frac{2\Gamma(n-3)}{\sqrt{\pi}|x|^3}$$
(64)

For $x^2 > 1$ (n = 3):

$$\sum_{l=0}^{\infty} \frac{\Gamma\left(\frac{1}{2} + l\right)}{\Gamma(1+l)} |x|^{-(2l+4)} - \sum_{l=1}^{\infty} \frac{\Gamma(l)}{\Gamma\left(\frac{1}{2} + l\right)} |x|^{-(2l+3)} + \frac{2\ln\left(\frac{|x|}{2}\right)}{\sqrt{\pi}|x|^3}$$
(65)

For $x^2 > 1$ (n > 3 and even):

$$\sum_{l=0}^{\infty} \frac{1}{(2l)!} \frac{\Gamma(n-1+2l)\Gamma\left(\frac{n-1+2l}{2}\right)}{\Gamma\left(\frac{n+2l}{2}\right)} \frac{|x|^{-(2l+n)}}{(3-n-2l)} + \sum_{l=(n-2)/2}^{\infty} \frac{\Gamma(1+2l)\Gamma(l)}{\Gamma\left(\frac{1}{2}+l\right)} \frac{|x|^{-(2l+3)}}{(3-n+2l)!} + \frac{2\Gamma(n-3)}{\sqrt{\pi}|x|^3}$$
(66)

For $x^2 > 1$ (n > 3 and odd):

$$-\sum_{l=0}^{\infty} \frac{1}{(2l+1)!} \frac{\Gamma(n+2l)\Gamma\left(\frac{n+2l}{2}\right)}{\Gamma\left(\frac{n+1+2l}{2}\right)} \frac{|x|^{-(2l+n+1)}}{(2-n-2l)}$$
$$-\sum_{l=(n-3)/2}^{\infty} \frac{\Gamma(1+2l)\Gamma(l)}{\Gamma\left(\frac{1}{2}+l\right)} \frac{|x|^{-(2l+3)}}{(3-n+2l)!} + \frac{2\Gamma(n-3)}{\sqrt{\pi}|x|^3}$$
(67)

4.2.3 Function
$$H_{4.4 \text{ yt}}^{2,3}\left(x^2, n\right)$$

From (41), we have that for $0 < x^2 < 1$, the required poles are identical to those in (57) and therefore satisfy the same multiplicity conditions. While for $x^2 > 0$, the poles are

$$\Gamma(1 - a_j - a_j v) \longrightarrow \alpha_1 = (n + l_1)/2$$

$$\alpha_2 = 3/2 + l_2$$

$$\alpha_3 = 3/2 + l_3$$
(68)

with $l_1, l_2, l_3 \in \mathbb{N}_0$ (keep this in mind). Here, we can get poles up to third order, which occur when $\alpha_1 = \alpha_2 = \alpha_3$. Since $\alpha_2 = \alpha_3$ for all l_2 and l_3 , these are always poles of at least second order. Thus, poles of third order occur when $\alpha_1 = \alpha_i$ (with i = 1, 2). The remaining poles α_1 are simple. Additionally, by comparing poles in (68) and (61), we can directly infer the multiplicity for poles in (68).

Therefore, if $n \notin \mathbb{Z}$, all poles α_1 are simple, while α_2 and α_3 are poles of second order, since $\alpha_2 = \alpha_3$. If $n \in \mathbb{Z}$, poles α_1 with l_1 satisfying $(n-3+l_1) \mod 2 = 0$ (where l_1 must be odd when nis even, and even when n is odd) are of third order, as do poles α_i with $l_i \ge (n-3)/2$. Consequently, poles α_1 are simple for any l_1 satisfying $(n-3+l_1) \mod 2 \neq 0$ (where l_1 must be odd when n is odd, and even when n is even), while α_i are poles of second order for $0 \le l_i < (n-3)/2$, since $\alpha_2 = \alpha_3$. In this case, if we consider n = 3, all α_2 and α_3 , and α_1 with l_1 even are poles of third order, while poles α_1 with l_1 odd are simple.

The corresponding expansions on each domain are given below, where $\gamma_0 = -\psi_0(1)$ represents the Euler-Mascheroni constant.

For $0 < x^2 < 1 (n > 2)$:

$$\frac{2^{n-3}}{\pi|x|} \sum_{k=0}^{\infty} \Gamma\left(\frac{n-1}{2} + k\right) \Gamma\left(\frac{n}{2} + k\right) \frac{x^{2k}}{((k+1)!)^2} \left[2\psi_0(2+k)\right]$$
Following the procedure described above (42) can be expressed as
$$-\psi_0\left(\frac{n-1}{2} + k\right) - \psi_0\left(\frac{n}{2} + k\right) - \ln\left(x^2\right) \left[(69) \right]$$

$$H_{2,2\Sigma}^{2,1}\left(x^2, n\right) = \frac{\Gamma(n-1)^2}{2^{n-1}\Gamma\left(n-\frac{1}{2}\right)|x|} f_0(x),$$

For $x^2 > 1$ (n > 2 and $n \notin \mathbb{Z})$:

$$2\sum_{l=0}^{\infty} \frac{(-1)^{l}}{l!} \frac{\Gamma(n-1+l)\Gamma\left(\frac{n-1+l}{2}\right)}{\Gamma\left(\frac{n+l}{2}\right)} \frac{|x|^{-(l+n)}}{(3-n-l)^{2}} + \frac{4\Gamma(n-3)}{\sqrt{\pi}|x|^{3}} \left(\ln\left(\frac{|x|}{2}\right) + \psi_{0}(n-3) + \gamma_{0}\right)$$
(70)

For $x^2 > 1$ (n = 3):

$$-4\sum_{l=0}^{\infty} \frac{\Gamma\left(\frac{3}{2}+l\right)}{\Gamma(1+l)} \frac{|x|^{-(2l+4)}}{(1+2l)^2} + \sum_{l=1}^{\infty} \frac{\Gamma(1+l)}{\Gamma\left(\frac{1}{2}+l\right)} \frac{|x|^{-(2l+3)}}{l^2} + \frac{2}{\sqrt{\pi}|x|^3} \left(\frac{\pi^2}{4} + \ln^2\left(\frac{|x|}{2}\right)\right)$$
(71)

For $x^2 > 1$ (*n* > 3 and even):

$$\sum_{l=0}^{\infty} \frac{2}{(2l)!} \frac{\Gamma(n-1+2l)\Gamma\left(\frac{n-1+2l}{2}\right)}{\Gamma\left(\frac{n+2l}{2}\right)} \frac{|x|^{-(2l+n)}}{(3-n-2l)^2} - \sum_{l=(n-2)/2}^{\infty} \frac{\Gamma(1+2l)\Gamma(1+l)}{\Gamma\left(\frac{1}{2}+l\right)} \frac{|x|^{-(2l+3)}}{l^2(3-n+2l)!} + \frac{4\Gamma(n-3)}{\sqrt{\pi}|x|^3} \left(\ln\left(\frac{|x|}{2}\right) + \psi_0(n-3) + \gamma_0\right)$$
(72)

For $x^2 > 1$ (n > 3 and odd):

$$-\sum_{l=0}^{\infty} \frac{2}{(2l+1)!} \frac{\Gamma(n+2l)\Gamma\left(\frac{n+2l}{2}\right)}{\Gamma\left(\frac{n+1+2l}{2}\right)} \frac{|x|^{-(2l+n+1)}}{(2-n-2l)^2} + \sum_{l=(n-3)/2}^{\infty} \frac{\Gamma(1+2l)\Gamma(1+l)}{l^2\Gamma\left(\frac{1}{2}+l\right)} \frac{|x|^{-(2l+3)}}{(3-n+2l)!} + \frac{4\Gamma(n-3)}{\sqrt{\pi}|x|^3} \left(\ln\left(\frac{|x|}{2}\right) + \psi_0(n-3) + \gamma_0\right)$$
(73)

4.3 Final expressions

In this section, we show that the power series derived in Sec. 4.2 can be simplified and expressed in terms of Gauss hypergeometric function ${}_{2}F_{1}$ (for more details on this function see e.g., Abramowitz & Stegun (1972), chapter 15). We begin with the series with domain $0 < x^2 < 1$, where the simplified expressions for (59) and (69) are obtained using Eq. (15.3.10) (from Abramowitz & Stegun (1972)), while for (63) we use Eq. (15.3.11) (from Abramowitz & Stegun (1972)). By applying Eq. (15.3.8) (from Abramowitz & Stegun (1972)) to each of the previous Gauss hypergeometric functions, we obtain the corresponding simplified expressions for the power series in the domain $x^2 > 1$. Then, we use Eq. (15.8.27) and Eq. (15.8.28) (from Abramowitz & Stegun (1972)) as appropriate, to get more compact expressions. Recall that for us n > 2, which is a physical constraint required by (1).

Following the procedure described above, the Fox H-function in (42) can be expressed as

$$H_{2,2\Sigma}^{2,1}\left(x^{2},n\right) = \frac{\Gamma\left(n-1\right)^{2}}{2^{n-1}\Gamma\left(n-\frac{1}{2}\right)|x|}f_{0}(x),\tag{74}$$

with

$$f_{0}(x) = \begin{cases} 2F_{1}\left(\frac{n-1}{2}, \frac{n}{2}; n - \frac{1}{2}; 1 - x^{2}\right) & \text{if } 0 < x^{2} < 1\\ 1 & \text{if } x^{2} = 1\\ \frac{1}{|x|^{n-1}} {}_{2}F_{1}\left(n-1, n-1; n - \frac{1}{2}; \frac{|x|-1}{2|x|}\right) & \text{if } x^{2} > 1 \end{cases}$$
 (75)

In the same way, the Fox H-function in (43) takes the form

$$H_{3,3\,M}^{2,2}\left(x^2,n\neq 3\right) = \frac{2\Gamma(n-3)}{\sqrt{\pi}|x|^3} - \frac{\Gamma\left(n-1\right)\Gamma\left(n-3\right)}{2^{n-3}\Gamma\left(n-\frac{3}{2}\right)|x|^3}f_1(x), \eqno(76)$$

with

$$f_{1}(x) = \begin{cases} 2F_{1}\left(\frac{n-3}{2}, \frac{n}{2} - 1; n - \frac{3}{2}; 1 - x^{2}\right) & \text{if } 0 < x^{2} < 1\\ 1 & \text{if } x^{2} = 1\\ \frac{1}{|x|^{n-3}} {}_{2}F_{1}\left(n - 3, n - 1; n - \frac{3}{2}; \frac{|x| - 1}{2|x|}\right) & \text{if } x^{2} > 1 \end{cases}$$

when $n \neq 3$, while for n = 3 we get

$$H_{3,3M}^{2,2}\left(x^{2}, n=3\right) = \frac{2}{\sqrt{\pi |x|^{3}}}$$

$$\left(\ln\left(\frac{|x|}{2}\right) + \frac{\arctan\left(\sqrt{1-x^{2}}\right)}{\sqrt{1-x^{2}}} \quad \text{if } 0 < x^{2} < 1\right)$$

$$\times \left\{1 - \ln(2) \quad \text{if } x^{2} = 1 \quad , \quad (78)$$

$$\ln\left(\frac{|x|}{2}\right) + \frac{\arctan\left(\sqrt{x^{2}-1}\right)}{\sqrt{x^{2}-1}} \quad \text{if } x^{2} > 1$$

which is the result of evaluating series (63) and (65).

For the Fox *H*-function in (44) we get an indetermination not only at n = 3, but also at n = 5/2. We remove the indetermination at n = 5/2 using the contiguous relation (15.2.27) (from Abramowitz & Stegun (1972)) in the domain $0 < x^2 < 1$. After that, we apply the procedure outlined at the beginning of this section to extend the result to the domain $x^2 > 1$. Thus, when $x \ne 3$ we get

$$\begin{split} H_{4,4\,\psi}^{2,3}\left(x^2,n\neq 3\right) &= \frac{4\Gamma(n-3)}{\sqrt{\pi}|x|^3} \left(\ln\left(\frac{|x|}{2}\right) + \psi_0(n-3) + \gamma_0\right) \\ &+ \frac{\Gamma\left(n-3\right)^2}{2^{n-4}\Gamma\left(n-\frac{3}{2}\right)|x|^5} \left[\left((2n-3)x^2-2\right)f_1(x) \right. \\ &+ \frac{n(n-1)(1-x^2)}{2n-3}f_2(x)\right], \end{split} \tag{79}$$

where $f_1(x)$ is given by (77) and

$$\begin{split} f_2(x) &= \\ &\times \begin{cases} 2F_1\left(\frac{n-3}{2},\frac{n}{2}-1;n-\frac{1}{2};1-x^2\right) & \text{if } 0 < x^2 < 1 \\ 1 & \text{if } x^2 = 1 \\ \frac{1}{|x|^{n-3}} {}_2F_1\left(n-3,n+1;n-\frac{1}{2};\frac{|x|-1}{2|x|}\right) & \text{if } x^2 > 1 \end{cases} , \quad (80) \end{split}$$

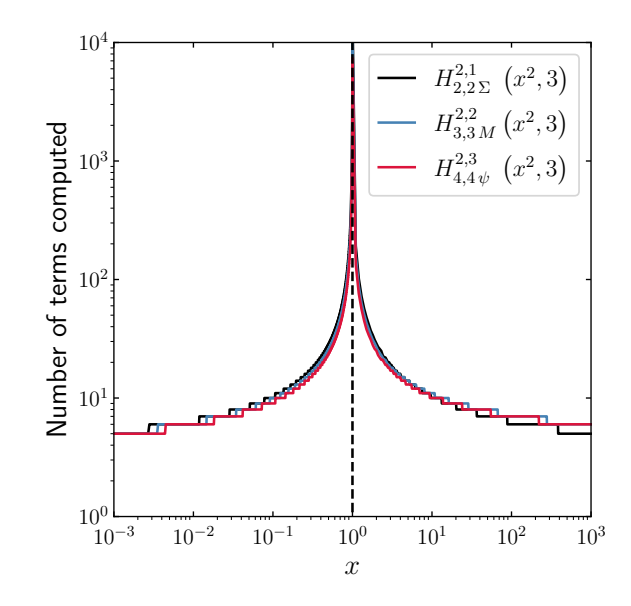


Figure 2. Number of terms required for the power series representations of the relevant Fox H-functions to converge. In this example we consider n = 3 and a tolerance of 10^{-15} .

while for n = 3 we get

$$H_{4,4\,\psi}^{2,3}\left(x^{2}, n=3\right) = \frac{2}{\sqrt{\pi}|x|^{3}}$$

$$\times \begin{cases} \ln^{2}\left(\frac{|x|}{2}\right) - \operatorname{arctanh}^{2}\left(\sqrt{1-x^{2}}\right) & \text{if } 0 < x^{2} < 1\\ \ln^{2}(2) & \text{if } x^{2} = 1\\ \ln^{2}\left(\frac{|x|}{2}\right) + \operatorname{arctan}^{2}\left(\sqrt{x^{2}-1}\right) & \text{if } x^{2} > 1 \end{cases}$$
(81)

which is the result of evaluating series (69) and (71).

4.4 Performance

As described above, we have simplified and expressed the Fox H-functions of interest in terms of simpler functions. Unfortunately, in general this is not possible, leaving the corresponding power series representations as a practical alternative. With this in mind, in this section we assess the accuracy and performance of the power series given in Sec. 4.2, demonstrating the value of working with the Fox H-function.

We start writing each power series in the form

$$S_N(x) \approx \sum_{k=0}^{N} C_k(x)$$
, with $S_{N+1}(x) = S_N(x) + C_{N+1}(x)$, (82)

where $C_k(x)$ denotes the k-th term of the given power series, and $S_N(x)$ represents the summation of the first N+1 terms. For instance, for the power series (59) we can write

$$C_k(x) = \frac{2^{n-3}}{\pi |x|} a_{1,k} x^{2k} \left(a_{2,k} - \ln\left(x^2\right) \right), \tag{83}$$

where we use the identities $\Gamma(k+1) = k\Gamma(k)$ and $\psi_0(k+1) = \psi_0(k) + 1/k$ to express the coefficients $a_{1,k}$ and $a_{2,k}$ recursively (for

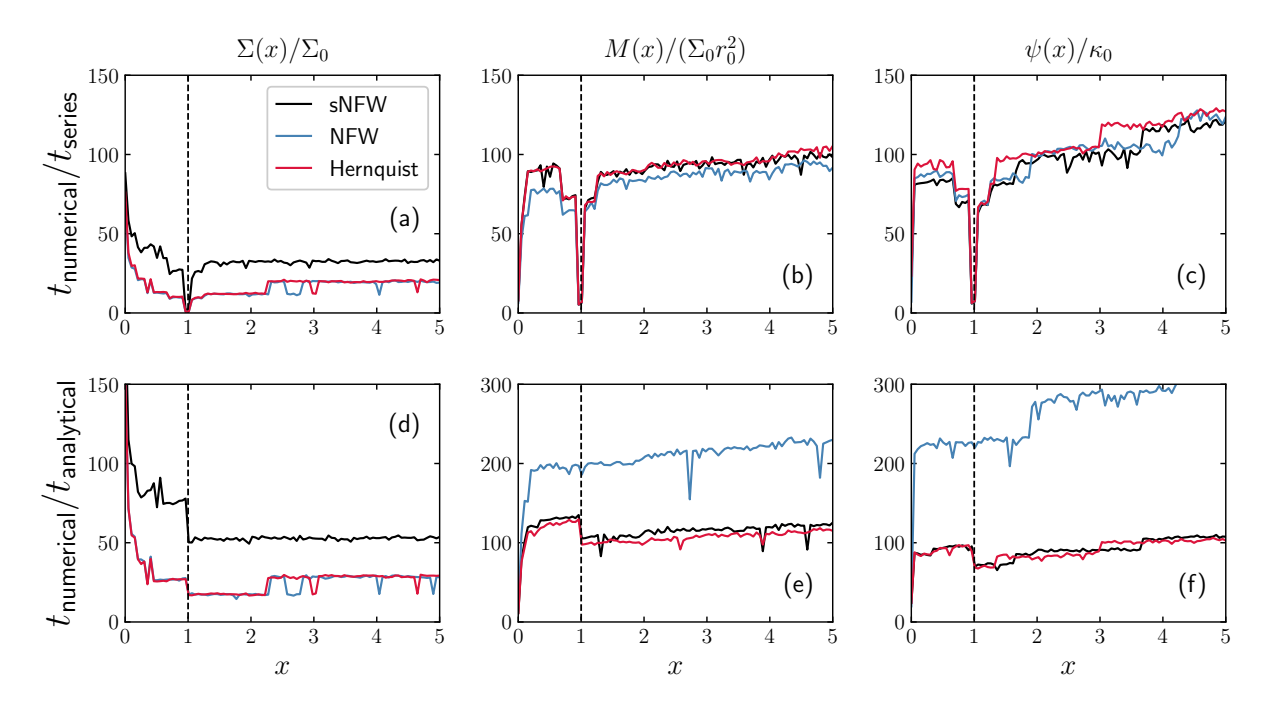


Figure 3. Computation time comparison between a direct numerical integration ($t_{numerical}$) and the power series approach (t_{series}) (upper row), and also between the numerical integration and the analytical expressions in Sec. 4.3 (lower row). The comparisons are depicted for the normalised surface mass density (left-hand column), normalised projected mass (middle column), and normalised deflection potential (right-hand column). In all panels the solid curves correspond to the sNFW (n = 7/2, black), NFW (n = 3, blue), and Hernquist (n = 4, red) lenses. The vertical dashed lines represent x = 1. The reported computation times represent averages over multiple realizations of each calculation to minimize numerical noise.

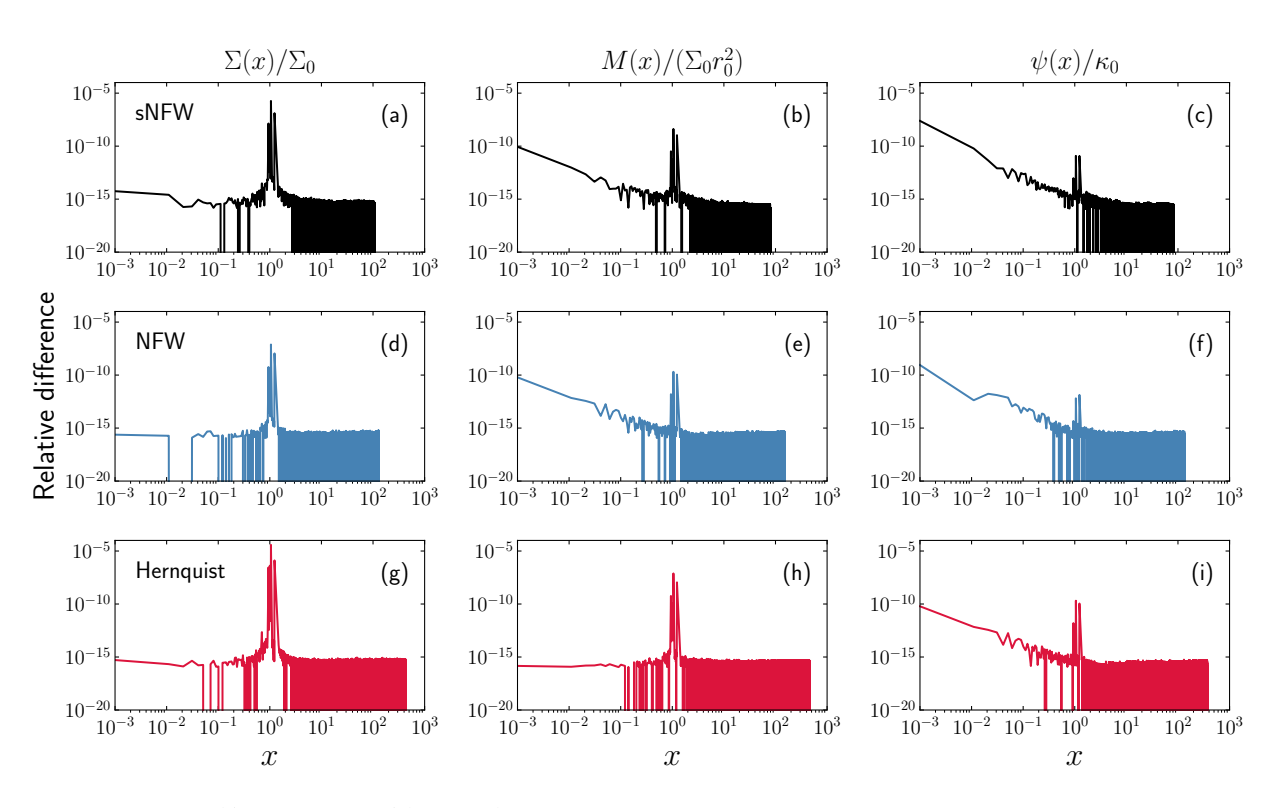


Figure 4. Relative difference | (series – analytical) / analytical | given for the normalised surface mass density (left-hand column), normalised projected mass (middle column), and normalised deflection potential (right-hand column). We show the relative difference for the sNFW (n = 7/2, black, upper row), NFW (n = 3, blue, middle row), and Hernquist (n = 4, red, lower row) lenses.

convenience) as

$$a_{1,k} = \begin{cases} \Gamma\left(\frac{n-1}{2}\right)\Gamma\left(\frac{n}{2}\right) & \text{if } k = 0\\ \frac{(2k+n-3)(2k+n-2)}{4k^2}a_{1,k-1} & \text{if } k > 0 \end{cases}$$
(84)

and

$$a_{2,k} = \begin{cases} 2\psi_0(1) - \psi_0\left(\frac{n-1}{2}\right) - \psi_0\left(\frac{n}{2}\right) & \text{if } k = 0\\ \frac{2}{k} - \frac{2}{2k+n-3} - \frac{2}{2k+n-2} + a_{2,k-1} & \text{if } k > 0 \end{cases}$$
 (85)

Now, the question is: when should we stop the summation? In this regard, we adopt an approach similar to the one used for the Gauss hypergeometric function in Pearson et al. (2017). We stop the summations once the three conditions $|C_N(x)/S_{N-1}(x)| < \text{tol}$, $|C_{N-1}(x)/S_{N-2}(x)| < \text{tol}$, and $|C_{N-2}(x)/S_{N-3}(x)| < \text{tol}$ are satisfied simultaneously for a given tolerance (tol).

Considering n=3 (NFW), Fig. 2 depicts the number of terms required for each summation to converge $(N_{\rm max}+1)$ as a function of x for the three Fox H-functions of interest, given a tolerance of 10^{-15} (which we use in this work unless otherwise stated). Since such functions are even, we restrict the domain in Fig. 2 to x>0. All three functions exhibit a similar behaviour, where the summations require about 10 terms when $x\ll 1$ and $x\gg 1$, while this number increases rapidly as $x\to 1$. This is expected, considering the discontinuity at $x^2=1$ in all three functions. For n=7/2 (sNFW) and n=4 (Hernquist) the number of terms required in each summation is also consistent with Fig. 2.

The imposed stopping conditions imply that $N_{\rm max}$ is unknown. Thus, every time we evaluate a Fox H-function, we must verify whether these stopping conditions are met, and we must repeatedly compute coefficients such as $a_{1,k}$ and $a_{2,k}$ in (83), even though they are independent of x. Therefore, this way of computing the different summations involved is accurate, but time consuming.

We can improve the computation time simply by fixing $N_{\rm max}$, which we can infer from the information given in Fig. 2. Nonetheless, in our case, we need to be careful because of how $N_{\rm max}$ behaves close to $x^2=1$. Then, if the domain of interest is not close to $x^2=1$, it is possible to choose a global $N_{\rm max}$. Otherwise, we can divide the domain into disjoint subsets and fix a different $N_{\rm max}$ for each subset. Therefore, from Fig. 2 and with n=3 (NFW), n=7/2 (sNFW), and n=4 (Hernquist) in mind, for the three Fox H-functions of interest we take $N_{\rm max}=50$ when $0 < x^2 < 0.5$ or $x^2 \ge 1.5$, $N_{\rm max}=200$ when $0.5 \le x^2 < 0.9$ or $1.1 \le x^2 < 1.5$, and $N_{\rm max}=10^4$ when $0.9 \le x^2 < 1$ or $1 < x^2 < 1.1$. Thus, with $N_{\rm max}$ in hand, we need to compute $a_{1,k}$ and $a_{2,k}$ only once, which leads to faster summations.

Now, in order to assess the performance of our approach, we use it to compute the lensing properties such as the surface mass density, projected mass, and deflection potential for the NFW, sNFW, and Hernquist lenses as they are given in equations (42)-(44). Then, we compare their computation times (t_{series}) against the results ($t_{numerical}$) obtained through direct numerical integration (where we use the method quad from scipy) applied to the lensing properties as defined in equations (3), (4), and (12). For both (4) and (12), we use the analytical representation of $\Sigma(x)$ obtained from (42) and (74) (as appropriate) instead of using the result of the numerical integration in (3). We do this because, for the surface mass density, it is usually possible to find an analytical expression. The ratio $t_{numerical}/t_{series}$ is depicted in Fig. 3 (upper row) as a function of the dimension less coordinate x, where we can see that, in general, for the surface mass

density (panel a) $t_{\rm numerical}/t_{\rm series} \gtrsim 10$, while for the projected mass (panel b) and deflection potential (panel c), $t_{\rm numerical}/t_{\rm series} \gtrsim 50$, where all three lenses show a similar behaviour. Overall, the power series approach outperforms the direct numerical integration; however, the power series performance drops when we get close to x=1 (vertical dashed lines). This behaviour is expected, considering the increase in the number terms needed for the power series to achieve a given tolerance.

Now, Fig. 3 (lower row) depicts the ratio $t_{\text{numerical}}/t_{\text{analytical}}$, which compares the computation time of the direct numerical integration with the analytical counterpart ($t_{\text{analytical}}$), which correspond to the expressions listed in Sec. 4.3. We use the implementation of Gauss hypergeometric function in scipy. In all three panels (d - f), we can see that, even though the analytical expressions are not given (in general) in terms of simple functions, they also outperform the numerical integration. However, for the projected mass (panel e) and deflection potential (panel f), the NFW (n=3, blue) shows a better performance compared to the other two lenses. This behaviour is a consequence of $H_{3,3\,M}^{2,2}$ (x^2 , x^2) (78) and $H_{4,4\,\psi}^{2,3}$ (x^2 , x^2) (81) being given in terms of inverse trigonometric and hyperbolic functions instead of the Gauss hypergeometric function (as justified in Sec. 4.3). With that being said, when no particular index x is of interest, the general results in Sec. 4.3 are practical.

If performance is a priority and it is clear what model to use (which index *n*), the best option is to take an extra step, and simplify (as much as possible) the required Fox *H*-functions using the results of either Sec. 4.2 or Sec. 4.3, aiming for expressions given in terms of more standard functions, which are usually easier to manipulate and faster to compute. For the NFW and Hernquist lenses such expressions are already known and are listed in Appendix D, whereas for the sNFW we provide the simplified expressions in Sec. 5.

Accuracy is also a relevant aspect when performing calculations. Here, we evaluate the accuracy of computing the lensing properties in terms of the power series representation by comparing with the corresponding simplified analytical expressions, where we use the relative difference |(series - analytical)/analytical|. In Fig. 4 we show the relative difference for the normalised surface mass density (left-hand column), normalised projected mass (middle column), and normalised deflection potential (right-hand column). For all three quantities, and for the three lens models as well, the highest relative difference (at most about 10^{-5}) occurs close to either x = 0 or x = 1, where as we know, our Fox H-functions are not well defined. Nonetheless, in general the relative difference is small, with a value of around 10^{-15} when we move away from x = 0 and x = 1. Therefore, there is no doubt that working with the power series representations of the Fox H-function is a good option, considering that when properly manipulated (as with any other power series), they provide accurate and considerably fast calculations.

5 THE SUPER-NFW AS A GRAVITATIONAL LENS

Considering the gNFW defined by (1), in Sec. 4 we found analytical expressions for its lensing properties (42)-(44), which are given in terms of the Fox H-function. Our goal in this section is to simplify such expressions (using either the power series in Sec. 4.2 or the analytical results in Sec. 4.3) for the particular case n = 7/2, or sNFW as it was named by Lilley et al. (2018a). As we argued is Sec. 4.4, this process is advantageous since analytical expressions given in terms of the simplest possible functions are generally faster to compute, and easier to work with.

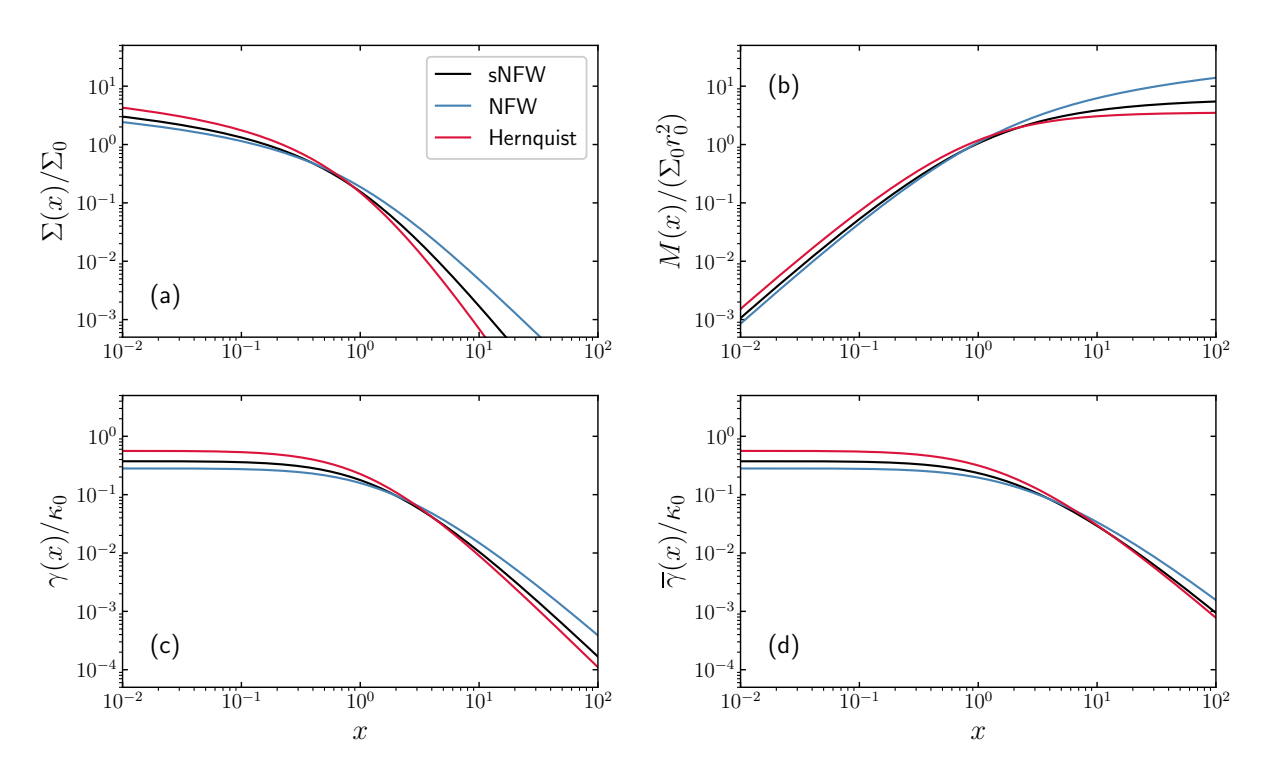


Figure 5. (a) Normalised surface mass density, (b) normalised projected mass, (c) normalised shear, and (d) normalised mean shear. In all panels the curves are given for the sNFW (black), NFW (blue), and Hernquist (red) lenses.

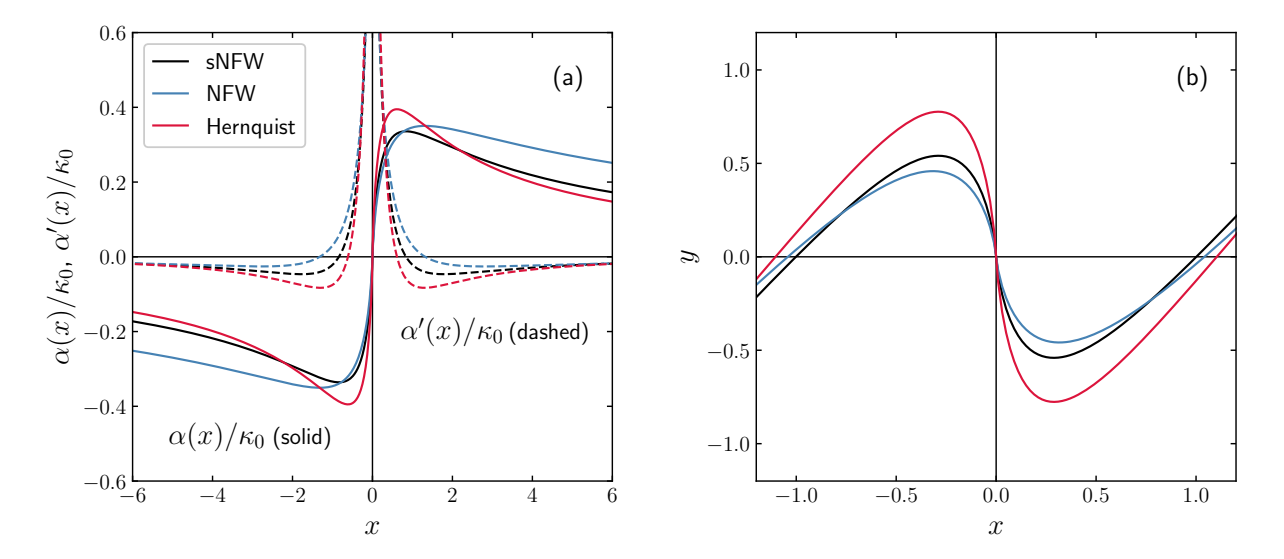


Figure 6. (a) Normalised deflection angle (solid curve) and its corresponding derivative (dashed curve). (b) Lens equation (5) given for $\kappa_0 = 3$. In both panels the curves are given for the sNFW (black), NFW (blue), and Hernquist (red) lenses.

We start with the surface mass density, which can be expresses as

$$\Sigma(x) = \Sigma_0 \begin{cases} \frac{9\pi}{128\sqrt{2}} & \text{if } x = 1\\ \frac{(3+x)K\left(\frac{1-x}{1+x}\right) - 4E\left(\frac{1-x}{1+x}\right)}{2(1-x)^2(1+x)^{3/2}} & \text{if } x \neq 1 \end{cases}$$
(86)

where K and E are the complete elliptic integrals of first and second kind, respectively. This result is equivalent to the expression reported by Lilley et al. (2018a). For the sNFW it is possible to find its surface

mass density directly from (3) without the need to use any fancy techniques (as it is the case with many profiles). If we use the surface mass density as given in (86), and try to find the projected mass and deflection potential from definitions (4) and (12), the integrals involved become too difficult to be solved by traditional means, or at least it is not evident how to proceed with the integration. Here, is where the use of the Fox H function comes handy. With that being said, for the projected mass and deflection potential the Fox H-function leads to

$$M(x) = 2\pi r_0^2 \Sigma_0 \begin{cases} 1 - \frac{3\pi}{8\sqrt{2}} & \text{if } x = 1\\ \frac{E\left(\frac{1-x}{1+x}\right) - xK\left(\frac{1-x}{1+x}\right)}{\sqrt{1+x}(x-1)} + 1 & \text{if } x \neq 1 \end{cases}$$
(87)

and

$$\psi(x) = 2\kappa_0 \left(\frac{2K\left(\frac{1-x}{1+x}\right)}{\sqrt{1+x}} + \ln\left(\frac{x}{8}\right) \right),\tag{88}$$

respectively. Since we are dealing with n > 3, according to (51) the sNFW possesses a finite mass. Together with (39), the characteristic surface mass density for the sNFW becomes $\Sigma_0 = M_{\infty}/(2\pi r_0^2)$, where M_{∞} represents its total mass. Recall that $\kappa_0 = \Sigma_0/\Sigma_{\rm cr}$ is the characteristic convergence.

We substitute these results into definitions (9) and (16) (as appropriate), and find the corresponding shear and mean shear, which can be written as

$$\gamma(x) = \kappa_0$$

$$\times \begin{cases} 2 - \frac{105\pi}{128\sqrt{2}} & \text{if } x = 1\\ \frac{x(4 - 3x - 5x^2)K\left(\frac{1 - x}{1 + x}\right) - 4(1 - 2x^2)E\left(\frac{1 - x}{1 + x}\right)}{x^2\sqrt{1 + x}(x - 1)} + \frac{2}{x^2} \end{cases}$$
(89)

and

$$\overline{\gamma}(x) = 2\kappa_0 \times \begin{cases} \frac{19\pi}{8\sqrt{2}} - 6\ln(2) - 1 & \text{if } x = 1\\ \frac{(5x - 4)K\left(\frac{1 - x}{1 + x}\right) - E\left(\frac{1 - x}{1 + x}\right)}{x^2\sqrt{1 + x}(x - 1)} + \frac{2}{x^2}\ln\left(\frac{x}{8}\right) - \frac{1}{x^2} & \text{if } x \neq 1 \end{cases}$$
(90)

respectively. From (50), we can see that both quantities satisfy $\gamma(0)/\kappa_0 = \overline{\gamma}(0)/\kappa_0 = 3/8$. Recall that for (86)-(90) we consider x > 0. Lastly, by substituting (87) into the general definition (6), the deflection angle takes the form

$$\alpha(x) = \frac{2\kappa_0}{x} \begin{cases} 1 - \frac{3\pi}{8\sqrt{2}} & \text{if } |x| = 1\\ \frac{E\left(\frac{1-|x|}{1+|x|}\right) - |x|K\left(\frac{1-|x|}{1+|x|}\right)}{\sqrt{1+|x|}(|x|-1)} + 1 & \text{if } |x| \neq 1 \end{cases}, \tag{91}$$

where the discontinuity at x = 0 is removable, with $\alpha(0) = 0$.

From Fig. 5 (panel a) it is evident that the surface mass density for the sNFW falls off asymptotically faster than for the NFW, but slower than for the Hernquist lens, which is consistent with how the profile (1) behaves. As a result, unlike the NFW, whose projected mass (Fig. 5 panel b) increases logarithmically and eventually diverges towards the outskirts, for the sNFW and Hernquist lenses, their projected mass tends asymptotically to a finite value (total mass), with the smallest being that of the Hernquist lens. Now, the distortions induced by the lens are stronger within the regions of higher density, thus, for the sNFW the shear and mean shear signals (Fig. 5 panel c and d, respectively) decrease faster than those of the Hernquist lens. Something similar happens for the deflection angle, as it is depicted in Fig. 6 (panel a). I summary, we have that towards the outskirts,

the lensing properties for the sNFW satisfy the condition of being in between properties of the NFW and Hernquist lenses, in agreement with the motivation for defining the sNFW as discussed in Lilley et al. (2018a).

5.1 Image formation and magnification

The non-linear nature of the lens equation opens the possibility of obtaining multiple images of the same source. Here, for the sNFW, we discuss how many images can be formed, and under which conditions. In that regard, Fig. 6 (panel b) depicts the lens equation with $\kappa_0 = 3$ for the sNFW (black), NFW (blue), and Hernquist (red) lenses, where it is clear that for these three models the features and behaviour of the lens equation are overall the same. For different values of κ_0 the main changes occur at the intersections (there are two of them) between the lens equation and the x-axis, which move closer or farther from the origin as κ_0 decreases or increases, respectively. Also, variations in κ_0 induce changes in amplitude, such that when the inner concave and convex sections of the lens equation disappear, it is no longer possible to obtain multiple images. Note that for many axisymmetric lenses their lens equation behaves similarly, with the exception of, for example, the point-like and SIS lenses (see e.g., Schneider et al. (2006)).

All information regarding image formation is summarised in Fig. 7 (panel a), where for simplicity, we restrict the radial coordinates to nonnegative values. Consider a point-like source at position $\mathbf{y}=(y,\varphi)$ on the source plane, where φ is its azimuthal coordinate. The black curve represents the lens equation, where the solid part corresponds to possible images on the lens plane at position $\mathbf{x}=(x,\varphi)$, while the dashed part corresponds to possible images at position $\mathbf{x}=(x,\varphi+\pi)$. The latter case is equivalent to the scenario in Fig. 6 (panel b) for x<0 and $y\geq0$.

The critical curves, at which the magnification $\mu(x)$ diverges, rule the presence of multiple images. The magnification is defined as

$$\frac{1}{\mu(x)} = (1 - \kappa(x))^2 - \gamma^2(x) = \frac{y(x)y'(x)}{x},\tag{92}$$

which leads to two possible critical curves. On the one hand, we have the tangential critical curve. This curve is a circle (also known as the Einstein ring) with radius x_{c1} , which satisfies

$$y(x)/x = 1 - \overline{\kappa}(x) = 0$$
, with $\overline{\kappa}(x) = \frac{\overline{\Sigma}(x)}{\Sigma_{cr}} = \frac{\alpha(x)}{x}$. (93)

This is basically the lens equation applied to a source with radial coordinate y = 0, but with the restriction $x \neq 0$. Although x = 0 is a solution to the lens equation, it does not represent a critical curve. On the other hand, we have the radial critical curve. This curve is a circle with radius x_{c2} , which satisfies

$$y'(x) = 1 - \alpha'(x) = 0. (94)$$

Here, by applying the Leibniz integral rule to the integral representation of $\alpha(x)$ in (6), we obtain $\alpha'(x) = 2\kappa(x) - \overline{\kappa}(x)$. Thus, x = 0 cannot represent a critical radial curve either.

Once we map the critical curves into the source plane, we get the caustic curves. These curves delimit the regions where a source will lead to multiple images. The tangential critical curve is mapped into $y_{c1}=0$, while the radial critical curve is mapped into a circle with radius y_{c2} . Critical and caustic curves are concentric. In Fig. 7 (panel a) the position of the critical curves and caustic curves are represented as vertical and horizontal solid black lines, respectively. For illustration, in Fig. 7 (panel b) we show an example of these curves for a sNFW lens with $\kappa_0=3$.

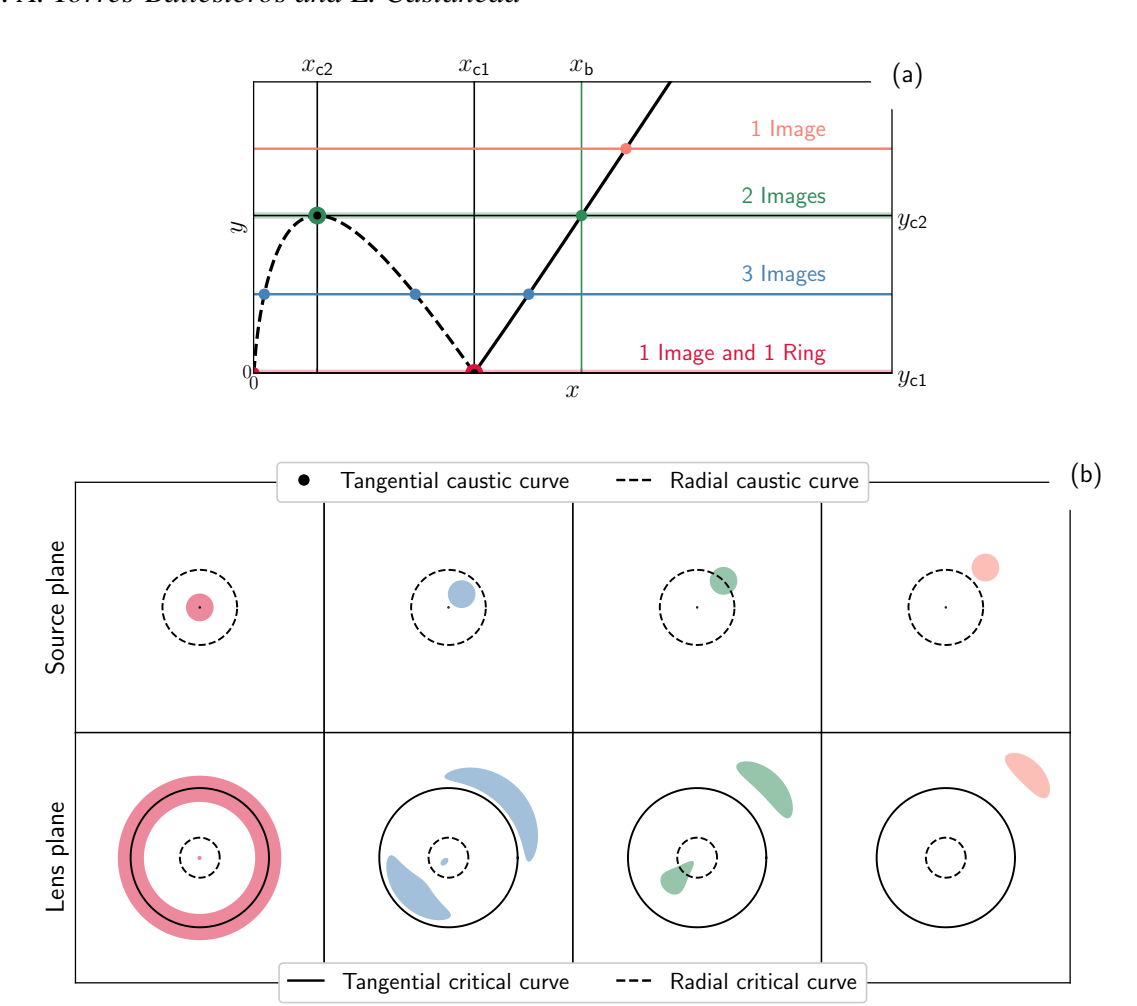


Figure 7. Image formation anatomy. In panel (a) the black curve represents the lens equation, such that for a source at position $\mathbf{y} = (y \ge 0, \varphi)$, it is possible to obtain images at position $\mathbf{x} = (x \ge 0, \varphi)$ (solid curve) or at position $\mathbf{x} = (x \ge 0, \varphi + \pi)$ (dashed curve). The vertical and horizontal black lines represent the position of critical and caustic curves, respectively. The additional horizontal lines show the possible scenarios for image formation depending on y, while the vertical green line at x_b represents the boundary within which multiple images can appear. Additionally, panel (b) shows an example of image formation for a sNFW lens, and an extended source with different positions relative to the caustic curves. Each colour matches one of the four scenarios described in panel (a).

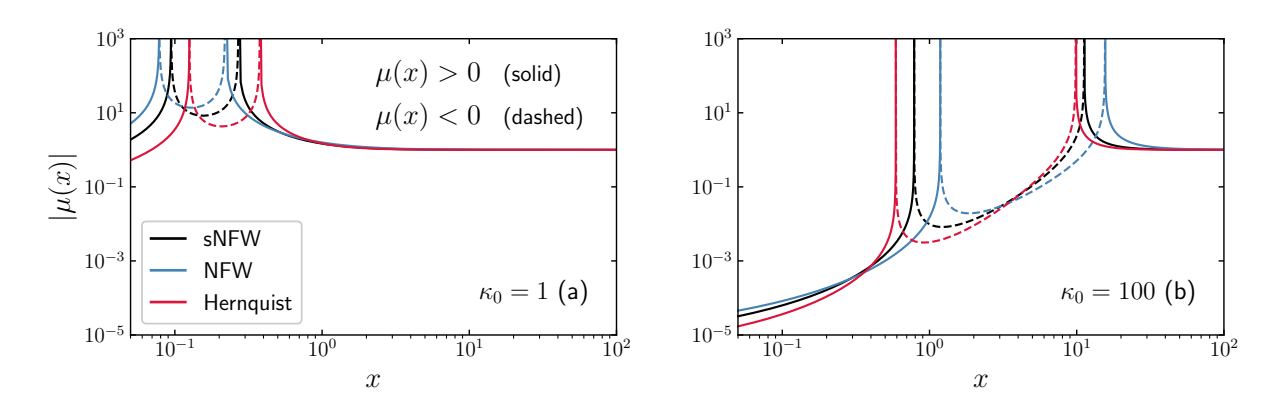


Figure 8. Absolute magnification $|\mu(x)|$ given for (a) $\kappa_0 = 1$ and (b) $\kappa_0 = 100$. In both panels the curves are given for the sNFW (black), NFW (blue), and Hernquist (red) lenses, where the solid and dashed curves correspond to $\mu(x) > 0$ and $\mu(x) < 0$, respectively.

Now, since $x_{c1} > x_{c2}$, the strong lensing effect can be produced as long as the tangential critical curve is present, which occurs when the characteristic convergence κ_0 is greater than a certain minimum ($\kappa_{0,\min}$). Given that the tangential critical curve satisfies $\overline{\kappa}(x) = \alpha(x)/x = 1$, once we make explicit $\alpha(x)$ and write κ_0 as a function of x, $\kappa_{0,\min}$ is the result of evaluating the limit when $x \to 0$ (no tangential critical curve is produced). In our case, from (6) and (43), for the gNFW lens we get

$$\kappa_0 = 1/\left(xH_{3,3M}^{2,2}\left(x^2, n\right)\right). \tag{95}$$

Thus, from either the power series representation (63), or the representations (76) (for $n \ne 3$) and (78) (for n = 3), it can be shown that $\kappa_{0,\min} = 0$. Therefore, any lens described by the gNFW produces a tangential critical curve if $\kappa_0 > 0$.

This result, however, does not apply to all profiles. For instance, if we consider a Non-Singular Isothermal Sphere (NIS) with core radius $r_C \neq 0$, from the expressions listed in Appendix C we can show that in this case $\kappa_{0,\min} = 1/\sqrt{\pi}$. Note that $\kappa_{0,\min}$ is subject to the definition of κ_0 , in particular when $\kappa_{0,\min} \neq 0$.

Returning to image formation, from Fig. 7 (panel a) we can see that for a source at y = 0 (horizontal red line) there are two possible solutions to the lens equation. These solutions correspond to the critical curve x_{c1} and one image at the centre (x = 0). At x = 0the magnification is finite and, for lenses with a divergent surface mass density like the gNFW, we have $\mu(x \to 0) = 0$. Such demagnified/faint image is difficult (if not impossible) to observe. For sources located at $0 < y < y_{c2}$ (horizontal blue line) we get three images. One of them is located at $x > x_{c1}$, while the other the two are located at $0 < x < c_{c1}$. Those two images merge at x_{c2} when the given source is located at y_{c2} , for which a second image is formed at $x > x_{c1}$ (horizontal green line). For sources located at $y > y_{c2}$ (horizontal orange line) only one image is formed at $x > x_{c1}$. Recall that, if the source has an azimuthal coordinate φ , the images with radial coordinate $0 < x < c_{c1}$ have azimuthal coordinate $\varphi + \pi$, while the images with radial coordinate $x > x_{c1}$ have azimuthal coordinate φ . As a final remark, in Fig. 7 (panel b) we illustrate these four possible scenarios of image formation for an extended source with radius 0.2 and a sNFW lens with $\kappa_0 = 3$.

Fig. 8 shows the absolute magnification $|\mu(x)|$ for the sNFW (black), NFW (blue), and Hernquist (red) lenses. These curves are given for $\kappa_0 = 1$ (panel a) and $\kappa_0 = 100$ (panel b). In terms of signed magnification, the solid and dashed curves represent $\mu(x) > 0$ and $\mu(x) < 0$, respectively. The morphological features exhibited by these curves are essentially the same for the three lenses of interest. The most evident similarity corresponds to two prominent vertical asymptotes, which represent the position of the critical curves. The inner one represents the radial critical curve, while the outer one represents the tangential critical curve. Therefore, images located at $x_{c2} < x < x_{c1}$ have negative parity, while images located at $0 < x < x_{c2}$ and $x > x_{c1}$ have positive parity. Also, we can see that, independently of κ_0 , the magnification satisfies $\mu(x) > 1$ for $x > x_{c1}$ (as expected). When comparing the magnifications, we can see that in general, in terms of magnitude, the magnification produced by the sNFW is larger than that of the Hernquist, but smaller than that of the NFW. The differences in magnitude are particularly evident within $x_{c2} < x < x_{c1}$. Moreover, there is a clear dependence on κ_0 . We can see that, within the region $0 < x < x_{c1}$, for these three models $|\mu(x)|$ decreases as κ_0 increases, producing demagnified images unless they are formed close to a critical curve.

Another relevant aspect to take into account, is how the critical and caustic curves behave as a function of κ_0 . In this regard, Fig. 9 (panel a) shows these curves simultaneously for the sNFW lens.

We can see that the critical curves move away from the centre, and the separation between critical curves increases, always satisfying $x_{c1} > x_{c2}$. We can also see that $x_{c2} > y_{c2}$ for small values of κ_0 , however, eventually this relation is reversed and we get $y_{c2} > x_{c2}$. For higher values of κ_0 , the radial critical and caustic curves keep increasing in size, but the radial caustic grows faster. This implies that when κ_0 increases it becomes easier to get multiple images, and since in terms of proportion the region within the radial critical curve is smaller, it is more likely to get a faint image close to the centre.

For the sNFW, NFW, and Hernquist lenses, the curves x_{c1} , x_{c2} , and y_{c2} as a function of κ_0 have a similar behaviour. In this regard, in Fig. 9 (panels b and c) we can see that for small values of κ_0 , the Hernquist lens produces larger critical curves than the other two lenses, but as κ_0 increases, the NFW takes its place and its critical curves start growing faster than those of the other two lenses (with the sNFW being in between). In particular, up to $\kappa_0 \sim 2$ the critical curves are comparable in size for the sNFW and NFW lenses, with the sNFW producing slightly larger curves, but as κ_0 increases they start getting apart from each other and this time the NFW produces significantly larger curves.

With respect to the caustic curves, for the three models the tangential caustic curve is always $y_{c1} = 0$, independently of κ_0 . For the radial caustic curves, we can see in Fig. 9 (panel d) that, independently of κ_0 , for the Hernquist lens its radial caustic curve is always larger and grows faster than those of the other two lenses, while the NFW always produces the smallest radial caustic curves. These results imply that it is much easier for the Hernquist or sNFW lenses to produce the strong lensing effect than it is for the NFW lens.

As a final remark on image formation, provided that sources are not located on caustics $(y \neq 0 \text{ and } y \neq y_{c2})$, we get either one or three images, in agreement with the odd images theorem. First explored in spherical galaxies by Dyer & Roeder (1980), and then generalised by Burke (1981), it requires lenses to have a non-singular mass distribution. However, it was shown by Bartelmann (1996) that a mass distribution such as the NFW, despite being singular at its centre, possesses a radial critical curve, forming an odd number of images. He argues that this is possible since $\alpha'(x)$ is continuous (for $(x > 0), \alpha'(x \to 0) = \infty$, and $\alpha'(x \to \infty) = 0$. This guaranties that there exists an x that satisfies (94). From the dashed curves in Fig. 6 (panel a) it is straightforward to see that these conditions are also fulfilled by the sNFW and Hernquist lenses. Additionally, as discussed in Mollerach & Roulet (2002), the appearance of an odd number of images can be argued from considering the deflection angle being bounded and continuous at x = 0. Alternatively, from the perspective of the deflection potential, theorem 1 in Petters & Werner (2010) indicates that the total number of images is given by $N = 2N_+ + g - 1$, where N_{+} is the number of images with positive parity, and g is the number of infinite singularities of ψ , which are those x_s for which $\psi(x \to x_s) = -\infty$. In our case, since g = 0, this theorem predicts N = 3 for sources with $0 < y < y_{c2}$, and N = 1 for sources with $y > y_{c2}$. Consequently, this suggests that the condition of the mass distribution being non-singular is more a sufficient than a necessary condition for obtaining an odd number of images.

5.2 Magnification invariant

When we have a source inside the caustic that produces the maximum possible number of images, $I = \sum_i \mu_i$ represents the sum of their corresponding (signed) magnifications. It has been shown that for certain simple lenses, I is constant and independent of most of their parameters. Therefore, it is usually referred to as the magnification invariant. That is the case, for example, of a system of n-point lenses

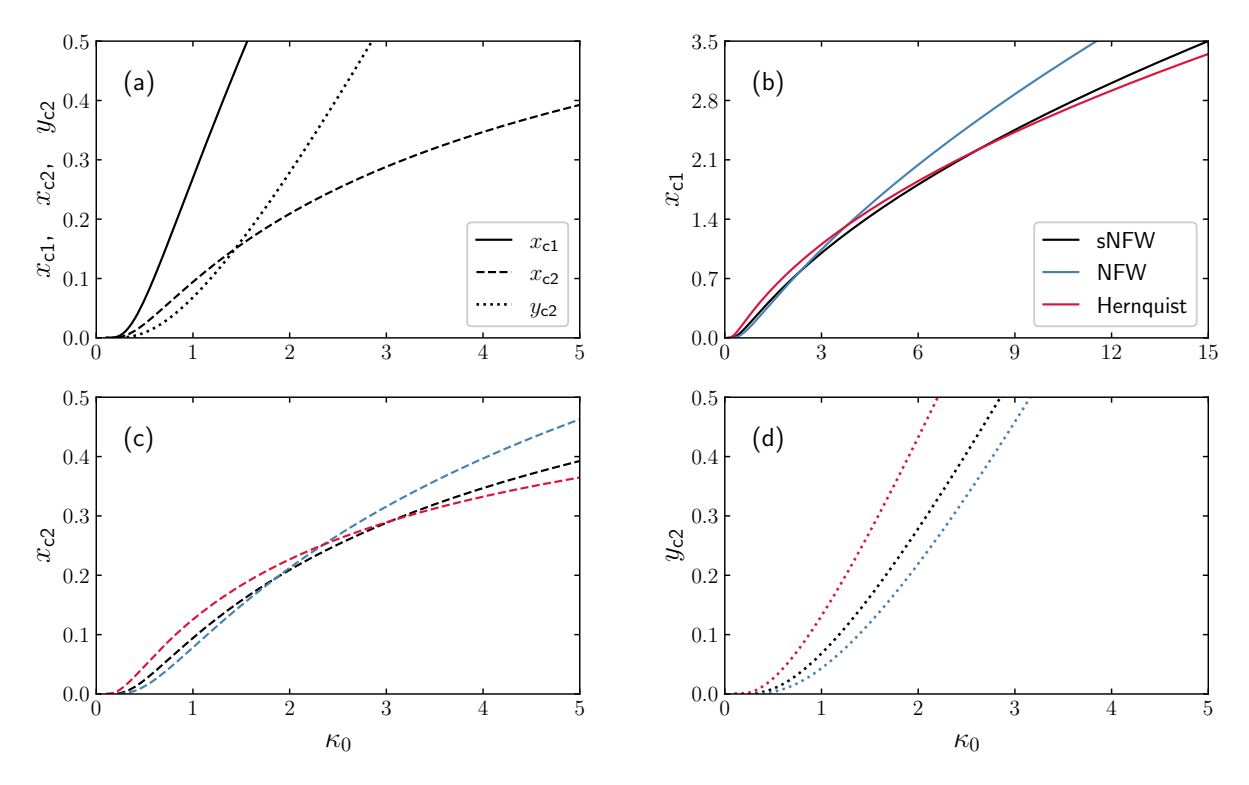


Figure 9. For the sNFW, panel (a) shows its tangential critical curve x_{c1} (solid), radial critical curve x_{c2} (dashed), and radial caustic curve y_{c2} (dotted) as a function of the characteristic convergence κ_0 . Additionally, panels (b)-(d) depict each of these curves for the sNFW (black), NFW (blue), and Hernquist (red) lenses. Note that for these lenses the tangential critical curve is formed as long as $\kappa_0 > 0$, and its corresponding caustic is $y_{c1} = 0$.

(Witt & Mao 1995; Rhie 1997), and the Plummer lens (Werner & Evans 2006), for which I=1, or the isothermal sphere for which I=2 (Dalal 1998; Wei et al. 2018). The magnification invariant has also been analytically computed for models intended to fit quadruple lenses, such as variations of the SIS model (Dalal 1998; Witt & Mao 2000; Dalal & Rabin 2001; Hunter & Evans 2001). More recently, Wei et al. (2018) have explored how I behaves for axisymmetric lenses such as the NFW, Einasto (for n=1/2, 1), an exponential disc, and the modified Hubble model, where they conclude that for such models I only depends on the characteristic convergence. However, as we discuss below, at least for the NFW, our numerical experiments suggest a more dynamical behaviour.

Here, we study how I behaves for the sNFW, NFW, and Hernquist lenses. For these three models we know that at most three images are formed, which occurs for sources within $0 < y < y_{c2}$. Each of these images appears inside one of three possible regions: region 1 $(0 < x < x_{c2})$, region 2 $(x_{c2} < x < x_{c1})$, and region 3 $(x_{c1} < x < x_b)$, where x_b (depicted as the vertical green line in Fig. 7 panel a) represents the outer boundary within which multiple images can form.

To evaluate I, we need to solve the lens equation (5) accurately. To do so, for a source located at y_0 , we take each of the three regions and construct a one-dimensional grid with N nodes and map all of them into the source plane by means of (5). Then, the node that is mapped closest to y_0 corresponds to the image within the corresponding region. The accuracy of this solution can be improved by using this value as an initial guess in some root finding method, as it could be Newton-Raphson. This is the approach applied by Wei et al. (2018). We opt for a refinement process instead, since the relative differences obtained are in general smaller. Nonetheless, from both approaches the behaviour exhibited by I is the same. We test this approach and our implementation by applying it to the NIS described in Appendix

C, for which Wei et al. (2018) showed that $I_{NIS} = 2$, independently of any parameter.

What we do here is, given a κ_0 , we solve the lens equation for multiple sources within $0 < y < y_{c2}$, and compute their corresponding I. We then compute its average value $\langle I \rangle$ and keep track of the variations by means of the maximum and minimum values achieved by I. We repeat this process for several values of κ_0 . In Fig. 10 (panel a) we can see the results for the NIS, where the solid curve represents $\langle I_{\rm NIS} \rangle$, and the variations in $I_{\rm NIS}$ are represented as a coloured band. From this figure it is clear that $\langle I_{\rm NIS} \rangle = 2$ for all κ_0 , and the variations on $I_{\rm NIS}$ are negligible (no coloured band). In fact, the highest variations with respect to the average that we get are around 10^{-10} . This behaviour is consistent with the analytical result. Therefore, our implementation works correctly.

Following the same procedure as for the NIS, we can see in Fig. 10 (panel b) that for the sNFW (black), NFW (blue), and Hernquist (red) lenses I is clearly not constant. We have that for these three lenses, $\langle I \rangle$ reaches a maximum within $1 < \kappa_0 < 10$, and then, it slowly decreases (showing a strong dependence on κ_0), in agreement with the results provided by Wei et al. (2018) for the NFW. However, our results differ from theirs regarding the constant nature of I for a fixed κ_0 . They concluded that I is approximately constant regardless of the position within the radial caustic. If we focus on the coloured bands in Fig. 10 (panel b), in general we can see a dynamical behaviour in I, where it is approximately constant only within a small domain. If, for example, we accept variations $|I_{\text{max}} - I_{\text{min}}|$ of at most 1% of the average value, it is fair to say that I is approximately constant when $4.5 < \kappa_0 < 7.8$ for the NFW, $3.5 < \kappa_0 < 6$ for the sNFW, and $2.4 < \kappa_0 < 4.3$ for the Hernquist lens. These intervals can be adjusted to meet observational uncertainties, and with that, it would

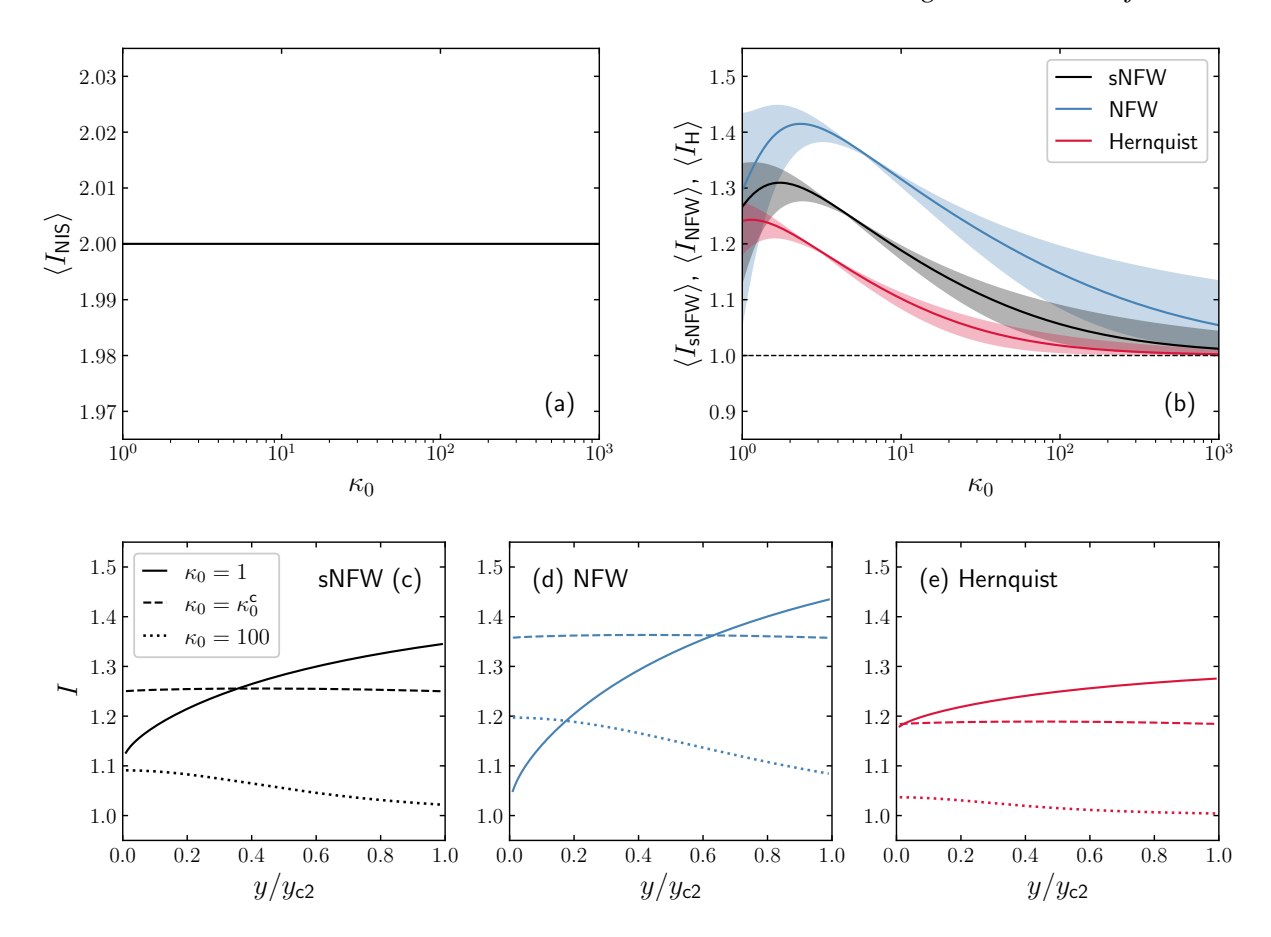


Figure 10. For a given characteristic convergence κ_0 , we evaluate I for multiple sources with radial position $0 < y < y_{c2}$ and compute the corresponding average $\langle I \rangle$. We repeat this process for several values of κ_0 . In panels (a) and (b) the solid curves denote $\langle I \rangle$, while the corresponding coloured bands enveloping these curves represent the range of possible values that I can have. On the one hand, in panel (a) we show $\langle I \rangle$ as a function of κ_0 for the NIS, where it is clear that $\langle I_{NIS} \rangle = 2$ and the variations in I are negligible (no coloured band), in agreement with the analytical result. On the other hand, in panel (b) we have $\langle I \rangle$ as a function of κ_0 for the sNFW (black), NFW (blue), and Hernquist (red). Here, the behaviour is more dynamical, which shows that I not only depends on κ_0 . We can see the variations in I for these three lenses in panels (c)-(e), where we show I as function of y/y_{c2} for $\kappa_0 = 1$ (solid), $\kappa_0 = \kappa_0^c$ (dashed), and $\kappa_0 = 100$ (dotted). I is constant for $\kappa_0 = \kappa_0^c$, however, the small deviations from a constant line that can be observed, are the result of the uncertainties in finding κ_0^c .

be possible to use I as an astrophysical tool for model selection, as it is discussed in e.g., Dalal (1998); Witt & Mao (2000).

For these three lenses, we observe that I is constant only for one κ_0 , which we denote κ_0^c . Its value is different for each model, where $\kappa_0^c \approx 5.9$ for the NFW, $\kappa_0^c \approx 4.5$ for the sNFW, and $\kappa_0^c \approx 3.1$ for the Hernquist lens. We can get a grasp on why this occurs from Fig. 10 (panels c - e). There, for $\kappa_0 = 1$ (solid) the minimum value that I can take (I_{\min}) occurs when $y \to 0$, whereas its maximum value (I_{\max}) occurs when $y \to y_{c2}$. However, this behaviour reverses when $\kappa_0 = 100$ (dotted), since I_{\min} occurs when $y \to y_{c2}$ and I_{\max} occurs when $y \to 0$. Therefore, during this transition from a small κ_0 to a large one, there exists a $\kappa_0 = \kappa_0^c$ for which $I_{\min} = I_{\max}$, indicating that I is constant. Furthermore, our numerical experiments suggest that for these three lenses $I_{\min} \to 1$ as κ_0 increases (dashed horizontal line), and $I \to 1$ as $\kappa_0 \to \infty$.

6 SUMMARY AND CONCLUSIONS

In this work, using of the Fox H-function we provide analytical expressions for the gravitational lensing properties of the gNFW profile (1) proposed by Evans & An (2006), where we focus on the sNFW (n = 7/2) (Lilley et al. 2018a) as an application case.

To achieve this, we provide a description of how we can write the projected mass and deflection potential in terms of the Fox H-function, whenever we have a lens whose surface mass density belongs to the family of lenses defined in (17). From these results, the corresponding convergence, deflection angle, shear, and mean shear can be derived straightforwardly. In particular, the lensing properties for the gNFW (42)-(44) are given in terms of three independent Fox H-functions.

This framework provides a simple way to obtain compact analytical expressions in terms of the Fox *H*-Function for the lensing properties of several axisymmetric lenses. Unfortunately, the Fox *H*-function has not been implemented yet in most programming languages (such as PYTHON, which is widely used in astronomy), making it difficult to use. Therefore, an efficient implementation of the Fox *H*-function would be beneficial. However, this task lies beyond the scope of this work. Instead, we compute the Fox *H*-function using its power series representation. A general description of the Fox *H*-function, including the relevant aspects used in this work, can be found in Appendix B.

For the gNFW, it was possible to simplify the required Fox *H*-functions in terms of the Gauss hypergeometric function, which is efficiently implemented in, for example, libraries like SCIPY. This simplification is not always possible (or at least not evident), making the power series representation an advantageous alternative to work with. In this regard, taking the gNFW as an example, in particular for

the sNFW, NFW, and Hernquist lenses, we compared the computation time between the power series approach and the direct numerical integration of the standard definition of the lensing properties. Our results show that when computing the surface mass density, as long as we avoid regions near x = 1, the power series approach is at least ten times faster than the direct numerical integration. Similarly, for the projected mass and deflection potential the power series approach is at least fifty times faster. Therefore, it is possible for the power series approach to outperforms the standard numerical integration.

We also tested the accuracy of such series representations, finding a relative difference of at most 10^{-5} near x = 0 and x = 1 (where the power series are indeterminate), and a relative difference of about 10^{-15} for x > 1. These results shows that the Fox *H*-function can be used as a reliable alternative to the standard numerical integration.

When a particular index n (model) is of interest, it is convenient to write its lensing properties in terms of simple and standard functions (if possible). These are usually easier to manipulate and faster to compute than either the Fox H-function or the Gauss hypergeometric function. We have done this for the sNFW, for which the required Fox H-functions reduce to expressions given in terms of the complete elliptic functions of first and second kind K and E, respectively. Its surface mass density (86) is equivalent to the expression reported by Lilley et al. (2018a), while its projected mass (87) and deflection potential (88) (which are fundamental to describe this axisymmetric lens) have not yet been reported in the literature. We also provide explicit analytical expressions for its deflection angle (91), shear (89), and mean shear (90). Compared to the NFW and Hernquist lenses, towards the outskirts of the lens, we found that the different lensing properties of the sNFW are between those of the NFW and Hernquist lenses, which is consistent with the expected behaviour of this profile as argued by Lilley et al. (2018a).

For sNFW, NFW, and Hernquist lenses, where each produce a maximum of three images, we evaluated the summation of their signed magnification I. For these lenses we found that, once we fix κ_0 , in general I exhibits a strong dependence on the position of the source inside the radial caustic. The variations are within a range $I_{\min} \leq I \leq I_{\max}$, where the boundaries depend on κ_0 . If we consider the average value $\langle I \rangle$, its dependence on κ_0 shows a behaviour consistent with what Wei et al. (2018) reported for the NFW, but our results differ on how I behaves for a fixed κ_0 . In fact, we found that I is constant only when $\kappa_0=\kappa_0^c$, where $\kappa_0^c\approx 5.9$ for the NFW, $\kappa_0^c\approx 4.5$ for the sNFW, and $\kappa_0^c\approx 3.1$ for the Hernquist lens. However, we can stablish a interval for κ_0 around κ_0^c for which I can be considered approximately constant (constrained by observational uncertainties). For example, considering deviations of at most 1% of the average value, we obtain $4.5 < \kappa_0 < 7.8$ for the NFW, $3.5 < \kappa_0 < 6$ for the sNFW, and $2.4 < \kappa_0 < 4.3$ for the Hernquist lens. Furthermore, our numerical experiments suggest that for these lenses $I_{\min} \rightarrow 1$ as κ_0 increases, and $I \to 1$ as $\kappa_0 \to \infty$. These properties are likely to be satisfied by any profile described by the gNFW.

We have shown that, in the context of gravitational lensing, the sNFW represents a reliable alternative to the NFW. In particular, if we consider that their lensing properties present similar behaviours, but with the advantage of the sNFW having a finite total mass. This results make the sNFW a good option for modelling dark matter halos or sub-halos in astrophysical lenses, not just at galactic scales, but also for galaxy groups and galaxy clusters. Additionally, it would be valuable to extend the analysis by considering an elliptical sNFW or including an external shear. It would also be interesting to study the magnification relations under this setting, and to explore if Imaintains its behaviour. However, these ideas lie beyond the scope of this paper, and we leave them for future work.

ACKNOWLEDGEMENTS

L. Castañeda was supported by Patrimonio Autónomo - Fondo Nacional de Financiamiento para la Ciencia, la Tecnología y la Innovación Francisco José de Caldas (MINCIENCIAS - COLOMBIA) Grant No. 110685269447 RC-80740-465-2020, projects 69723. We would like the thank the anonymous referee for the thoughtful report, which helped to improve the clarity of the paper.

DATA AVAILABILITY

The figures presented in this work can be reproduced with the scripts available at https://github.com/torres-daniel/Gravitational-lensing-bythe-super-NFW.

```
REFERENCES
Abramowitz M., Stegun I. A., 1972, Handbook of Mathematical Functions
Baes M., Gentile G., 2011, A&A, 525, A136
Baes M., van Hese E., 2011, A&A, 534, A69
Bartelmann M., 1995, A&A, 303, 643
Bartelmann M., 1996, A&A, 313, 697
Bartelmann M., Schneider P., 2001, Phys. Rep., 340, 291
Burke W. L., 1981, ApJ, 244, L1
Dalal N., 1998, ApJ, 509, L13
Dalal N., Rabin J. M., 2001, Journal of Mathematical Physics, 42, 1818
Dyer C. C., Roeder R. C., 1980, ApJ, 238, L67
Ellis R. S., 2010, Philosophical Transactions of the Royal Society of London
    Series A, 368, 967
Evans N. W., An J. H., 2006, Phys. Rev. D, 73, 023524
Fox C., 1961, Transactions of the American Mathematical Society, 98, 395
Freundlich J., et al., 2020, MNRAS, 499, 2912
Giocoli C., Meneghetti M., Metcalf R. B., Ettori S., Moscardini L., 2014,
    MNRAS, 440, 1899
Hernquist L., 1990, ApJ, 356, 359
Hinshaw G., Krauss L. M., 1987, ApJ, 320, 468
Hoekstra H., Jain B., 2008, Annual Review of Nuclear and Particle Science,
    58, 99
Hunter C., Evans N. W., 2001, ApJ, 554, 1227
Hurtado R., Castañeda L., Tejeiro J. M., 2014, International Journal of
    Astronomy and Astrophysics, 4, 340
Huterer D., 2010, General Relativity and Gravitation, 42, 2177
Jullo E., Kneib J. P., Limousin M., Elíasdóttir Á., Marshall P. J., Verdugo T.,
    2007, New Journal of Physics, 9, 447
Keeton C. R., 2001, arXiv e-prints, pp astro-ph/0102341
Kilbas A. A., 2004, H-transforms: Theory and Applications. CRC press
Kilbas A. A., Saigo M., 1999, Journal of Applied Mathematics and Stochastic
    Analysis, 12, 191
Lilley E. J., Evans N. W., Sanders J. L., 2018a, MNRAS, 476, 2086
Lilley E. J., Sanders J. L., Evans N. W., Erkal D., 2018b, MNRAS, 476, 2092
Martel H., Shapiro P. R., 2003, arXiv e-prints, pp astro-ph/0305174
Massey R., Kitching T., Richard J., 2010, Reports on Progress in Physics, 73,
```

Mollerach S., Roulet E., 2002, Gravitational lensing and microlensing. World

Munshi D., Valageas P., van Waerbeke L., Heavens A., 2008, Phys. Rep., 462,

Nakajima R., Bernstein G. M., Fadely R., Keeton C. R., Schrabback T., 2009,

Natarajan P., Williams L. L. R., Bradač M., Grillo C., Ghosh A., Sharon K.,

Miralda-Escude J., 1991, ApJ, 370, 1

Scientific, doi:10.1142/4890

Wagner J., 2024, Space Sci. Rev., 220, 19

Navarro J. F., Frenk C. S., White S. D. M., 1997, ApJ, 490, 493

ApJ, 697, 1793

Oguri M., 2010, PASJ, 62, 1017

Oguri M., 2021, PASP, 133, 074504

Pearson J. W., Olver S., Porter M. A., 2017, Numerical Algorithms, 74, 821 Petters A. O., Werner M. C., 2010, General Relativity and Gravitation, 42, 2011

Retana-Montenegro E., van Hese E., Gentile G., Baes M., Frutos-Alfaro F., 2012a, A&A, 540, A70

Retana-Montenegro E., Frutos-Alfaro F., Baes M., 2012b, A&A, 546, A32 Rhie S. H., 1997, ApJ, 484, 63

Schneider P., Ehlers J., Falco E. E., 1992, Gravitational Lenses. Springer, doi:10.1007/978-3-662-03758-4

Schneider P., Kochanek C., Wambsganss J., 2006, Gravitational lensing: strong, weak and micro: Saas-Fee advanced course 33. Springer, doi:https://doi.org/10.1007/978-3-540-30310-7

Umetsu K., 2020, A&A Rev., 28, 7

Wei C.-L., Chu Z., Shu Y.-P., 2018, Research in Astronomy and Astrophysics, 18 080

Werner M. C., Evans N. W., 2006, MNRAS, 368, 1362

Witt H. J., Mao S., 1995, ApJ, 447, L105

Witt H. J., Mao S., 2000, MNRAS, 311, 689

APPENDIX A: THE MELLIN TRANSFORM TECHNIQUE

Given a function f, its Mellin transform is an integral transformation defined as

$$F(u) = \mathfrak{M}_f(u) = \int_0^\infty f(x) x^{u-1} dx,$$
 (A1)

where $u \in \mathbb{C}$. Likewise, the inverse Mellin transform of F takes the

$$f(x) = \mathfrak{M}_F^{-1}(x) = \frac{1}{2\pi i} \int_{\mathcal{L}} F(u) x^{-u} du,$$
 (A2)

with \mathcal{L} being parallel to the imaginary axis in the complex plane.

Now, if f can be written as the Mellin convolution $(f_1 \star f_2)(x)$ of two functions, namely f_1 and f_2 , which reads

$$f(x) = (f_1 \star f_2)(x) = \int_0^\infty t^{-1} f_1(t) f_2(x/t) dt, \tag{A3}$$

its Mellin transform turns out to be

$$F(u) = \mathfrak{M}_{f_1 \star f_2}(u)$$

$$= \int_0^\infty (f_1 \star f_2)(x) x^{u-1} dx$$

$$= \int_0^\infty f_1(t) \left(\int_0^\infty f_2(x/t) x^{u-1} t^{-1} dx \right) dt, \tag{A4}$$

where, if we consider h = x/t, it is easy to show that

$$F(u) = \mathfrak{M}_{f_1 \star f_2}(u) = \mathfrak{M}_{f_1}(u)\mathfrak{M}_{f_2}(u). \tag{A5}$$

Finally, by applying the inverse Mellin transform (A2) to (A5), it

$$f(x) = \mathfrak{M}_F^{-1}(x) = \frac{1}{2\pi i} \int_{\mathcal{L}} \mathfrak{M}_{f_1}(u) \mathfrak{M}_{f_2}(u) x^{-u} du, \tag{A6}$$

which smoothly leads to the definition of the Fox H-function when \mathfrak{M}_{f_1} and \mathfrak{M}_{f_2} are given as the product of Gamma functions, as we discuss in Appendix B.

APPENDIX B: THE FOX H-FUNCTION

The Fox H-function was first introduced in Fox (1961) as the generalisation of the Meijer G-function.

Here, we provide the definition and properties of the Fox H-function that are needed to describe the gNFW profile as a gravitational lens. For a more comprehensive description of the Fox H-function, refer to e.g., Kilbas & Saigo (1999); Kilbas (2004). The Fox H-function is in general a complex-valued function defined by the Mellin-Barnes integral

$$H_{p,q}^{m,n}(x) = H_{p,q}^{m,n} \left[x \middle| (a_1, A_1), \dots, (a_p, A_p) \middle| (b_1, B_1), \dots, (b_q, B_q) \right]$$
$$= \frac{1}{2\pi i} \int_{\Gamma} \Theta(u) x^{-u} du$$
(B1)

with

$$\Theta(u) = \frac{\prod_{j=1}^{m} \Gamma(b_j + B_j u) \prod_{j=1}^{n} \Gamma(1 - a_j - A_j u)}{\prod_{j=n+1}^{p} \Gamma(a_j + A_j u) \prod_{j=m+1}^{q} \Gamma(1 - b_j - B_j u)},$$
 (B2)

where $m, n, p, q \in \mathbb{N}_0$, A_j (j = 1, ..., p) and B_j (j = 1, ..., q) are positive real numbers, while a_j (j = 1, ..., p) and b_j (j = 1, ..., q)are complex numbers. From the properties of the Γ function, we have that the poles present in (B2) correspond to the points where the Γ functions in its numerator diverge, which occurs when their argument equals zero or a negative integer. Therefore, the contour \mathcal{L} separates the poles of the product $\prod_{j=1}^{m} \Gamma(b_j + B_j u)$ from those of the product $\prod_{i=1}^{n} \Gamma(1 - a_j - A_j u)$. In the special case $A_j = 1$ and $B_j = 1$, the Fox H-function reduces to the Meijer G-function

$$G_{p,q}^{m,n}(x) = G_{p,q}^{m,n} \left[x \begin{vmatrix} a_1, \dots, a_p \\ b_1, \dots, b_q \end{vmatrix} \right].$$

Following Kilbas & Saigo (1999), we evaluate the Fox H-function using its power series expansion. This series expansion depends on the multiplicity of the different poles β_i (of functions $\Gamma(b_i + B_i u)$) and poles α_i (of functions $\Gamma(1 - a_i - A_i u)$), which are given as

$$\beta_j = -\left(\frac{b_j + k_j}{B_j}\right) \quad (j = 1, \dots, m \quad \text{and} \quad k_j \in \mathbb{N}_0)$$
 (B3)

$$\alpha_j = \frac{1 - a_j + l_j}{A_j} \quad (j = 1, \dots, n \quad \text{and} \quad l_j \in \mathbb{N}_0).$$
 (B4)

Considering the parameters

$$\Delta = \sum_{j=1}^{q} B_j - \sum_{j=1}^{p} A_j \quad \text{and} \quad \delta = \prod_{j=1}^{q} B_j^{B_j} \prod_{j=1}^{p} A_j^{-A_j},$$
 (B5)

the power series expansion converges when (see Theorems 2 - 6 in Kilbas & Saigo (1999))

Case 1:
$$\Delta > 0$$
 and $x \neq 0$, or $\Delta = 0$ and $0 < |x| < \delta$. (B6a)

Case 2:
$$\Delta < 0$$
 and $x \neq 0$, or $\Delta = 0$ and $|x| > \delta$. (B6b)

Thus, in both cases, the power series expansion of the Fox H-function can be expressed as

$$H_{p,q}^{m,n}(x) = \underbrace{\sum_{i} \sum_{k_i} C_{1i} x^{-u_{pi}}}_{\text{Simple poles}}$$

+
$$\sum_{k_1} C_2 x^{-u_{p_1}} \left(C_2' - \ln(x) \right)$$
Second order poles

$$+ \underbrace{\sum_{k_1} C_3 x^{-u_{p_1}} \left(\frac{1}{2} C_3^{\prime 2} + \frac{1}{2} C_3^{\prime \prime} - C_3^{\prime} \ln(x) + \frac{1}{2} \ln^2(x) \right)}_{\text{(B7)}},$$

where we have considered the expansion for poles up to third order. In particular, we make explicit the possibility of having several Γ functions with simple poles, while for higher order poles we only consider the possibility of having one pair or triplet of Γ functions with poles of second or third order, respectively. This is what we face in this work, however, for poles of second or third order, if more than one pair or triplet of Γ functions with poles of these orders appear, we can add a new summation (one for each extra pair or triplet) with the same functional form as in (B7). Kilbas & Saigo (1999) provide the general expansion for poles of arbitrary order, which reduces to (B7) after some algebra.

The form taken by the coefficients C_s , C_s' , and C_s'' (with s = 1, 2, 3 as appropriate) in (B7), depends on each of the aforementioned cases, which we make explicit below. Here, the prime does not denote derivative.

Case 1 (B6a): In this case the poles of interest are those given by (B3). At most m of them are simple poles, which we denote $u_{pi} = \beta_i$ (i = 1, ..., m at most). The corresponding coefficients take the form

$$C_{1i} = \frac{(-1)^{k_i}}{B_i k_i!} \frac{\prod_{\substack{j=1\\j\neq i}}^{m} \Gamma(b_j + B_j \beta_i) \prod_{j=1}^{n} \Gamma(1 - a_j - A_j \beta_i)}{\prod_{j=n+1}^{p} \Gamma(a_j + A_j \beta_i) \prod_{j=m+1}^{q} \Gamma(1 - b_j - B_j \beta_i)}.$$
 (B8)

For poles of higher order we have $u_{p1} = \beta_1$, where $\beta_1 = \beta_2$ for poles of second order and $\beta_1 = \beta_2 = \beta_3$ for poles of third order. These relations allow us to write k_2 and k_3 in terms of k_1 , such that, for s = 2, 3 the corresponding coefficients are

$$C_{s} = \left(\prod_{j=1}^{s} \frac{(-1)^{k_{j}}}{B_{j}k_{j}!}\right) \frac{\prod_{j=s+1}^{m} \Gamma(b_{j} + B_{j}\beta_{1}) \prod_{j=1}^{n} \Gamma(1 - a_{j} - A_{j}\beta_{1})}{\prod_{j=n+1}^{p} \Gamma(a_{j} + A_{j}\beta_{1}) \prod_{j=m+1}^{q} \Gamma(1 - b_{j} - B_{j}\beta_{1})},$$
(B9)

$$C'_{s} = \sum_{j=s+1}^{m} B_{j} \psi_{0}(b_{j} + B_{j}\beta_{1}) - \sum_{j=1}^{n} A_{j} \psi_{0}(1 - a_{j} - A_{j}\beta_{1})$$

$$- \sum_{j=n+1}^{p} A_{j} \psi_{0}(a_{j} + A_{j}\beta_{1}) + \sum_{j=m+1}^{q} B_{j} \psi_{0}(1 - b_{j} - B_{j}\beta_{1})$$

$$+ \sum_{j=1}^{s} B_{j} \psi_{0}(1 + k_{j}), \tag{B10}$$

and

$$C_{3}^{"} = \sum_{j=4}^{m} B_{j}^{2} \psi_{1}(b_{j} + B_{j}\beta_{1}) + \sum_{j=1}^{n} A_{j}^{2} \psi_{1}(1 - a_{j} - A_{j}\beta_{1})$$

$$- \sum_{j=n+1}^{p} A_{j}^{2} \psi_{1}(a_{j} + A_{j}\beta_{1}) - \sum_{j=m+1}^{q} B_{j}^{2} \psi_{1}(1 - b_{j} - B_{j}\beta_{1})$$

$$+ \sum_{j=1}^{3} B_{j}^{2} \left(\frac{\pi^{2}}{3} - \psi_{1}(1 + k_{j})\right). \tag{B11}$$

Case 2 (B6b): In this case the poles of interest are those given by (B4). At most n of them are simple poles, which we denote $u_{pi} = \alpha_i$

 $(i = 1 \dots n \text{ at most})$. The corresponding coefficients take the form

$$C_{1i} = \frac{(-1)^{l_i}}{A_i l_i!} \frac{\prod_{j=1}^{m} \Gamma(b_j + B_j \alpha_i) \prod_{\substack{j=1 \ j \neq i}}^{n} \Gamma(1 - a_j - A_j \alpha_i)}{\prod_{\substack{j=n+1 \ j = m+1}}^{p} \Gamma(a_j + A_j \alpha_i) \prod_{\substack{j=m+1 \ j = m+1}}^{q} \Gamma(1 - b_j - B_j \alpha_i)}, \quad (B12)$$

For poles of higher order we have $u_{p1} = \alpha_1$, where $\alpha_1 = \alpha_2$ for poles of second order and $\alpha_1 = \alpha_2 = \alpha_3$ for poles of third order. These relations allow us to write l_2 and l_3 in terms of l_1 , such that, for s = 2, 3 the corresponding coefficients are

$$C_{s} = -\left(\prod_{j=1}^{s} \frac{(-1)^{l_{j}-1}}{A_{j}l_{j}!}\right) \frac{\prod_{j=1}^{m} \Gamma(b_{j} + B_{j}\alpha_{1}) \prod_{j=s+1}^{n} \Gamma(1 - a_{j} - A_{j}\alpha_{1})}{\prod_{j=n+1}^{p} \Gamma(a_{j} + A_{j}\alpha_{1}) \prod_{j=m+1}^{q} \Gamma(1 - b_{j} - B_{j}\alpha_{1})},$$
(B13)

$$C'_{s} = \sum_{j=1}^{m} B_{j} \psi_{0}(b_{j} + B_{j}\alpha_{1}) - \sum_{j=s+1}^{n} A_{j} \psi_{0}(1 - a_{j} - A_{j}\alpha_{1})$$

$$- \sum_{j=n+1}^{p} A_{j} \psi_{0}(a_{j} + A_{j}\alpha_{1}) + \sum_{j=m+1}^{q} B_{j} \psi_{0}(1 - b_{j} - B_{j}\alpha_{1})$$

$$- \sum_{j=1}^{s} A_{j} \psi_{0}(1 + l_{j}), \tag{B14}$$

and

$$C_{3}^{"} = \sum_{j=1}^{m} B_{j}^{2} \psi_{1}(b_{j} + B_{j}\alpha_{1}) + \sum_{j=4}^{n} A_{j}^{2} \psi_{1}(1 - a_{j} - A_{j}\alpha_{1})$$

$$- \sum_{j=n+1}^{p} A_{j}^{2} \psi_{1}(a_{j} + A_{j}\alpha_{1}) - \sum_{j=m+1}^{q} B_{j}^{2} \psi_{1}(1 - b_{j} - B_{j}\alpha_{1})$$

$$+ \sum_{i=1}^{3} A_{j}^{2} \left(\frac{\pi^{2}}{3} - \psi_{1}(1 + l_{j})\right). \tag{B15}$$

As a final remark, when working with the power series (B7), it s useful to keep in mind that

$$\lim_{x \to -k} \frac{1}{\Gamma(1+x)} = \frac{1}{\Gamma(1-k)} = 0,$$
(B16)

$$\lim_{x \to -k} \frac{\psi_0(1+x)}{\Gamma(1+x)} = \frac{\psi_0(1-k)}{\Gamma(1-k)} = (-1)^k \Gamma(k), \tag{B17}$$

$$\lim_{x \to -k} \frac{\psi_1(1+x)}{\Gamma(1+x)^2} = \frac{\psi_1(1-k)}{\Gamma(1-k)^2} = \Gamma(k)^2,$$
(B18)

APPENDIX C: A SIMPLE APPLICATION CASE

Consider a Singular Isothermal Sphere (SIS) whose mass density is given by

$$\rho_{\rm SIS}(r) = \frac{\sigma_{\nu}^2}{2\pi G r^2},\tag{C1}$$

where σ_v is the velocity dispersion, and G is the gravitational constant. Its corresponding surface mass density, given in terms of the Abel integral (31) (in analogy to (32)) reads

$$\Sigma_{\text{SIS}}(x) = \frac{\sigma_v^2}{\pi G \xi_0} \int_x^\infty \frac{dt}{t \sqrt{t^2 - x^2}},\tag{C2}$$

with $t = r/\xi_0$, where in this case the normalisation scale length ξ_0 could be, for example, the Einstein radius. When we write (C2) as the Mellin convolution (A3) between $f_{1,SIS}$ and $f_{2,SIS}$, we have that

$$f_{1,SIS}(h=t) = \frac{\sigma_v^2}{\pi G \xi_0},\tag{C3}$$

for which its Mellin transform $\mathfrak{M}_{f_1, \mathrm{SIS}}$ (see (A1)) does not converge. This result is enough to conclude that (C2) cannot be written as (A6), and, in consequence, it cannot be given in terms of the Fox H-Function. At least, not by this mean.

We can add a core with radius r_c by means of $r^2 \rightarrow r^2 + r_c^2$, forming a Non-Singular Isothermal Sphere (NIS) whose mass density is

$$\rho_{\text{NIS}}(r) = \frac{\sigma_{\nu}^2}{2\pi G \left(r^2 + r_c^2\right)}.$$
 (C4)

This mass distribution is simple enough to be described as a gravitational lens by direct integration, as shown in Hinshaw & Krauss (1987). For this reason, it is a good exercise to describe it in terms of the Fox *H*-function. In particular, doing this exercise helps us to become familiar with the series expansion (B7).

Following the same process that we applied for the gNFW in Sec. 4, and by taking the normalisation scale length $\xi_0 = r_c$, it can be shown without much trouble that for the NIS, its surface mass density can be written as the Mellin convolution (see (A3)) between

$$f_{1,\text{NIS}}(t=b) = \frac{\sigma_v^2}{\pi G r_c} \frac{t^2}{t^2 + 1}$$
 (C5)

and $f_{2,NIS}$, which turns out to be identical to (34). Their corresponding Mellin transforms (see (A1)) are

$$\mathfrak{M}_{f_1,\,\text{NIS}}(u) = -\frac{\sigma_v^2}{2\pi G r_c} \Gamma\left(1 - \frac{u}{2}\right) \left(\frac{u}{2}\right) \tag{C6}$$

and (36), respectively. Therore, from (A6) and using the change of variable v = 1 + u/2 (for convenience), the surface mass density becomes

$$\Sigma_{\text{NIS}}(x) = \Sigma_0^{\text{NIS}} x \left(\frac{1}{2\pi i} \int_C \Theta_{\Sigma}^{\text{NIS}}(v) x^{-2v} dv \right), \tag{C7}$$

with

$$\Theta_{\Sigma}^{\text{NIS}}(\nu) = \Gamma\left(-\frac{1}{2} + \nu\right)\Gamma(1 - \nu) \tag{C8}$$

and

$$\Sigma_0^{\text{NIS}} = \frac{\sigma_v^2}{2\sqrt{\pi}Gr_c},\tag{C9}$$

where it is clear that (C7) satisfies (17) for a = 1 and b = 2. Thus, from (C8) along with the outline given in Sec. 3, we can write the surface mass density, projected mass, and deflection potential explicitly in terms of the Fox H-function (B1) as

$$\Sigma_{\text{NIS}}(x) = \Sigma_0^{\text{NIS}} x H_{1,1}^{1,1} \left[x^2 \middle| \frac{(0,1)}{(-\frac{1}{2},1)} \right], \tag{C10}$$

$$M_{\text{NIS}}(x) = \pi r_c^2 \Sigma_0^{\text{NIS}} x^3 H_{2,2}^{1,2} \left[x^2 \begin{vmatrix} (0,1), (-\frac{1}{2},1) \\ (-\frac{1}{2},1), (-\frac{3}{2},1) \end{vmatrix},$$
(C11)

$$\psi_{\text{NIS}}(x) = \frac{\kappa_0^{\text{NIS}} x^3}{2} H_{3,3}^{1,3} \left[x^2 \left| \frac{(0,1),(-\frac{1}{2},1),(-\frac{1}{2},1)}{(-\frac{1}{2},1),(-\frac{3}{2},1),(-\frac{3}{2},1)} \right. \right], \tag{C12}$$

respectively.

From parameters (B5), we can show that the three Fox H-functions in (C10)-(C12) satisfy $\Delta=0$ and $\delta=1$. Hence, as described in B6, they converge for $0 < x^2 < 1$ and $x^2 > 1$. Therefore, considering that for us x>0, and by applying the power series representation (B7), we get

$$\Sigma_{\text{NIS}}(x) = \Sigma_0^{\text{NIS}} \begin{cases} \sum_{k=0}^{\infty} \frac{(-1)^k}{k!} \Gamma\left(\frac{1}{2} + k\right) x^{2k} & \text{if } 0 < x < 1\\ \sum_{l=0}^{\infty} \frac{(-1)^l}{l!} \Gamma\left(\frac{1}{2} + l\right) x^{-2l-1} & \text{if } x > 1 \end{cases}$$
(C13)

$$M_{\text{NIS}}(x) = \pi r_c^2 \Sigma_0^{\text{NIS}} \times \begin{cases} \sum_{k=0}^{\infty} \frac{(-1)^k}{(1+k)!} \Gamma\left(\frac{1}{2} + k\right) x^{2k+2} & \text{if } 0 < x < 1 \\ 2\sum_{l=0}^{\infty} \frac{(-1)^l}{l!} \Gamma\left(\frac{1}{2} + l\right) \frac{x^{-2l+1}}{(1-2l)} - 2\sqrt{\pi} & \text{if } x > 1 \end{cases}, \quad (C14)$$

$$\psi_{\text{NIS}}(x) = \frac{\kappa_0^{\text{NIS}}}{2}$$

$$\begin{cases} \sum_{k=0}^{\infty} \frac{(-1)^k}{k!} \Gamma\left(\frac{1}{2} + k\right) \frac{x^{2k+2}}{(1+k)^2} & \text{if } 0 < x < 1 \\ 4 \sum_{l=0}^{\infty} \frac{(-1)^l}{l!} \Gamma\left(\frac{1}{2} + l\right) \frac{x^{-2l+1}}{(1-2l)^2} - 4\sqrt{\pi} \left(\ln\left(\frac{x}{2}\right) + 1\right) & \text{if } x > 1 \end{cases}$$
(C15)

The discontinuities at x = 0 and x = 1 in (C13)-(C15) are removable, so that for $x \ge 0$ it can be shown that they converge to

$$\Sigma_{\text{NIS}}(x) = \frac{\sqrt{\pi}\Sigma_0^{\text{NIS}}}{\sqrt{1+x^2}},\tag{C16}$$

$$M_{\text{NIS}}(x) = 2\pi^{3/2} r_c^2 \Sigma_0^{\text{NIS}} \left(\sqrt{1 + x^2} - 1 \right), \tag{C17}$$

$$\psi_{\text{NIS}}(x) = 2\sqrt{\pi}\kappa_0^{\text{NIS}}\left(\sqrt{1+x^2} - \ln\left(\frac{1+\sqrt{1+x^2}}{2}\right) - 1\right),$$
 (C18)

respectively. For this application case, it is worth noting that in all cases the Fox H-function coincides with the Meijer G-function. From these results, and using definitions (9) and (11), we can write the corresponding shear and mean shear as

$$\gamma_{\text{NIS}} = \sqrt{\pi} \kappa_0 \left(\frac{2 + x^2 - 2\sqrt{1 + x^2}}{x^2 \sqrt{1 + x^2}} \right) \tag{C19}$$

and

$$\overline{\gamma}_{\text{NIS}}(x) = \frac{2\sqrt{\pi}\kappa_0^{\text{NIS}}}{x^2} \left(\sqrt{1+x^2} - 2\ln\left(\frac{1+\sqrt{1+x^2}}{2}\right) - 1 \right),$$
 (C20)

respectively. Similarly, from (6) the deflection angle takes the form

$$\alpha_{\text{NIS}}(x) = \frac{2\sqrt{\pi}\kappa_0^{\text{NIS}}}{x} \left(\sqrt{1+x^2} - 1\right),$$
 where $\alpha_{\text{NIS}}(0) = 0$. (C21)

APPENDIX D: NFW AND HERNOUIST

In this appendix, for the NFW and Hernquist profiles we list their analytical properties as gravitational lenses (see e.g, Bartelmann (1996); Keeton (2001)). For this task, we use the auxiliary functions

$$f(x) = \begin{cases} \operatorname{arccosh}\left(\frac{1}{x}\right) & \text{if } 0 < x < 1\\ \operatorname{arccos}\left(\frac{1}{x}\right) & \text{if } x > 1 \end{cases}$$
 (D1)

and

$$s(x) = \begin{cases} 1 & \text{if } 0 < x < 1 \\ -1 & \text{if } x > 1 \end{cases}$$
 (D2)

which help us to get compact expressions. It can be shown that with the appropriate value of n, (42)-(44) along with (6), (9) and (16) reduce to the expressions given below. Note that, with the exception of the deflection angle, these expressions are valid for x > 0.

D1 NFW

Here, the characteristic surface mass density is $\Sigma_0^{\rm NFW}=2\sqrt{\pi}\rho_0r_0$, where ρ_0 is a characteristic density and r_0 is a scale length. With this, we can write

$$\Sigma_{\text{NFW}}(x) = \frac{\Sigma_0^{\text{NFW}}}{\sqrt{\pi}} \begin{cases} \frac{1}{3} & \text{if } x = 1\\ \frac{1}{x^2 - 1} \left(1 - \frac{f(x)}{\sqrt{|1 - x^2|}} \right) & \text{if } x \neq 1 \end{cases}, \tag{D3}$$

$$M_{\rm NFW}(x) = 2\sqrt{\pi}r_0^2\Sigma_0^{\rm NFW} \begin{cases} 1-\ln(2) & \text{if } x=1\\ \ln\left(\frac{x}{2}\right) + \frac{f(x)}{\sqrt{|1-x^2|}} & \text{if } x\neq1 \end{cases}, \tag{D4}$$

$$\psi_{\rm NFW}(x) = \frac{\kappa_0^{\rm NFW}}{\sqrt{\pi}} \begin{cases} \ln^2{(2)} & \text{if } x = 1\\ \ln^2{(\frac{x}{2})} - s(x)f^2(x) & \text{if } x \neq 1 \end{cases}, \tag{D5}$$

 $\gamma_{\rm NFW}(x) = \kappa_0^{\rm NFW}/(\sqrt{\pi}x^2)$

$$\times \begin{cases}
\frac{5}{3} - 2\ln(2) & \text{if } x = 1 \\
2\ln\left(\frac{x}{2}\right) + \frac{x^2}{1 - x^2} + \frac{(2 - 3x^2)s(x)f(x)}{(|1 - x^2|)^{3/2}} & \text{if } x \neq 1
\end{cases} , \tag{D6}$$

 $\overline{\gamma}_{NFW}(x) = 2\kappa_0^{NFW}/(\sqrt{\pi}x^2)$

$$\times \begin{cases}
\ln^{2}(2) + \ln(2) - 1 & \text{if } x = 1 \\
\ln^{2}\left(\frac{x}{2}\right) - \ln\left(\frac{x}{2}\right) - s(x)f^{2}(x) - \frac{f(x)}{\sqrt{|1 - x^{2}|}} & \text{if } x \neq 1
\end{cases} , \tag{D7}$$

and

$$\alpha_{\rm NFW}(x) = \frac{2\kappa_0^{\rm NFW}}{\sqrt{\pi}x} \begin{cases} 1 - \ln(2) & \text{if } |x| = 1\\ \ln\left(\frac{|x|}{2}\right) + \frac{f(|x|)}{\sqrt{|1 - x^2|}} & \text{if } |x| \neq 1 \end{cases}, \tag{D8}$$

where $\alpha_{NFW}(0) = 0$.

D2 Hernquist

Here, the characteristic surface mass density is $\Sigma_0^{\rm H} = M_{\infty}/(2\sqrt{\pi}r_0^2)$, where M_{∞} is the total mass of the distribution and r_0 is a scale length. With this, we can write

$$\Sigma_{\rm H}(x) = \frac{\Sigma_0^{\rm H}}{\sqrt{\pi}} \begin{cases} \frac{4}{15} & \text{if } x = 1\\ \frac{1}{(x^2 - 1)^2} \left(\frac{(2 + x^2) f(x)}{\sqrt{|1 - x^2|}} - 3 \right) & \text{if } x \neq 1 \end{cases}, \tag{D9}$$

$$M_{\rm H}(x) = 2\sqrt{\pi}r_0^2 \Sigma_0^{\rm H} \begin{cases} \frac{1}{3} & \text{if } x = 1\\ \frac{x^2}{x^2 - 1} \left(1 - \frac{f(x)}{\sqrt{|1 - x^2|}}\right) & \text{if } x \neq 1 \end{cases}, \tag{D10}$$

$$\psi_{\rm H}(x) = \frac{2\kappa_0^{\rm H}}{\sqrt{\pi}} \begin{cases} 1 - \ln{(2)} & \text{if } x = 1\\ \ln{\left(\frac{x}{2}\right)} + \frac{f(x)}{\sqrt{|1 - x^2|}} & \text{if } x \neq 1 \end{cases},\tag{D11}$$

$$\gamma_{\rm H}(x) = \frac{\kappa_0^{\rm H}}{\sqrt{\pi}} \begin{cases} \frac{2}{5} & \text{if } x = 1\\ \frac{1 + 2x^2}{(x^2 - 1)^2} - \frac{3x^2 f(x)}{(11 - x^2)^{5/2}} & \text{if } x \neq 1 \end{cases}$$
(D12)

$$\overline{\gamma}_{H}(x) = 2\kappa_{0}^{H}/(\sqrt{\pi}x^{2})$$

$$\times \begin{cases} \frac{5}{3} - 2\ln(2) & \text{if } x = 1\\ 2\ln\left(\frac{x}{2}\right) + \frac{x^{2}}{1 - x^{2}} + \frac{(2 - 3x^{2})s(x)f(x)}{(|1 - x^{2}|)^{3/2}} & \text{if } x \neq 1 \end{cases}$$
(D13)

and

$$\alpha_{\rm H}(x) = \frac{2\kappa_0^{\rm H}}{\sqrt{\pi}x} \begin{cases} \frac{1}{3} & \text{if } |x| = 1\\ \frac{x^2}{x^2 - 1} \left(1 - \frac{f(|x|)}{\sqrt{|1 - x^2|}}\right) & \text{if } |x| \neq 1 \end{cases},$$
 (D14)

where $\alpha_{\rm H}(0) = 0$

This paper has been typeset from a T_EX/L^2T_EX file prepared by the author.